Quantifying erosion in a pre-Alpine catchment at high resolution with concentrations of cosmogenic ^{10}Be, ^{26}Al, and ^{14}C

Chantal Schmidt[1,2], David Mair[1], Naki Akçar[1], Marcus Christl[3], Negar Haghipour[3], Christof Vockenhuber[3], Philip Gautschi[3], Brian McArdell[2], Fritz Schlunegger[1]

[1] Institute of Geology, University of Bern, Bern, 3012, Switzerland
[2] Swiss Federal Research Institute WSL, Birmensdorf, 8903, Switzerland
[3] Laboratory of Ion Beam Physics, ETH Zurich, Zürich, 8093, Switzerland

Correspondence to: Chantal Schmidt (chantal.schmidt@unibe.ch)

Abstract

Quantifying erosion across spatial and temporal scales is essential for assessing different controlling mechanisms and their contribution to long-term sediment production. However, the episodic supply of material through landsliding complicates quantifying the impact of the individual erosional mechanisms at the catchment scale. To address this, we combine the results of geomorphic mapping with measurements of cosmogenic ^{10}Be, ^{26}Al, and ^{14}C concentrations in detrital quartz. The sediments were collected in a dense network of nested sub-catchments within the 12 km^2-large Gürbe basin that is situated at the northern margin of the Central European Alps of Switzerland. The goal is to quantify the denudation rates, disentangle the contributions of the different erosional mechanisms (landsliding versus overland flow erosion) to the sedimentary budget of the study basin, and to trace the sedimentary material from source to sink. In the Gürbe basin, spatial erosion patterns derived from ^{10}Be and ^{26}Al concentrations indicate two distinct zones: the headwater zone with moderately steep hillslopes dominated by overland flow erosion, with high nuclide concentrations and low denudation rates (~ 0.1 mm/yr), and the steeper lower zone shaped by deep-seated landslides. Here lower concentrations correspond to higher denudation rates (up to 0.3 mm/yr). In addition, ^{26}Al/^{10}Be ratios in the upper zone align with the surface production ratio of these isotopes (6.75), which is consistent with sediment production through overland flow erosion. In the lower zone, higher ^{26}Al/^{10}Be ratios of up to 8.8 point towards sediment contribution from greater depths, which characterises the landslide signal. The presence of a knickzone in the river channel at the border between the two zones points to the occurrence of a headward migrating erosional front and supports the interpretation that the basin is undergoing a long-term transient response to post-glacial topographic changes. In this context, erosion rates inferred from ^{10}Be and ^{26}Al isotopes are consistent, suggesting a near-steady, possibly self-organised sediment production regime over the past several thousand years. In such a regime, individual and stochastically operating landslides result in the generation of an aggregated signal that is recorded as a higher average denudation rate by the cosmogenic isotopes. Although in-situ ^{14}C measurements were also conducted, the resulting concentrations are difficult to interpret as soil mixing (due to landsliding), sediment storage or an increase in erosion rates might influence the ^{14}C concentration pattern in a yet non-predictable way.

1 Introduction

In alpine environments stochastic processes such as landslides often drive sediment production and condition the occurrence of debris flows (Kober et al., 2012; Clapuyt et al., 2019). During periods of strong hillslope-channel coupling, the processes operating on the hillslopes deliver detrital material to the channel network, where sediment from various sources becomes mixed and transported downstream. As a consequence, the sediments at the outlet of such a catchment are a mixture of detrital material generated through a large variety of erosional mechanisms in different locations in the upstream basin. This makes it challenging to allocate the detrital material and to quantify how the different sub-catchments and erosional processes have contributed to the overall sediment budget (Battista et al., 2020). This is particularly the case for those basins that are underlain by a homogenous bedrock lithology, which prevents the identification of different sediment sources using petrologic fingerprinting methods (e.g., Stutenbecker et al., 2018). In such a context, in-situ ^{10}Be has proven a useful tool to quantify the generation of sediment through erosion (Bierman and Steig, 1996; vonBlanckenburg, 2005) across a large range of catchment sizes – from small headwater basins (~1 km^2; Granger et al., 1996) to major river systems such as the Ganges and Amazon rivers (Wittmann et al., 2009; Dingle et al., 2018). In addition, ^{10}Be-derived denudation rates have also been successfully applied to explore the controls of various parameters on surface erosion such as: topography and rock strength (DiBiase et al., 2010; Carr et al., 2023), environmental conditions (Reber et al., 2017; Starke et al., 2020), rock uplift as well as climatic variables including precipitation (Roda-Boluda et al., 2019; Chittenden et al., 2014), runoff and runoff variability (Savi et al., 2015), and frost cracking processes (Delunel et al., 2010; Savi et al., 2015). However, a successful ^{10}Be-based assessment of basin-averaged denudation rates requires that the material at the sampling site is well mixed (Binnie et al., 2006), representing the contributions from the various tributary basins according to the rates at which sediment has been generated in them. In catchments where sediment has been episodically supplied e.g., by landslides, denudation rate estimates may be biased towards the impact of a specific sediment source (Bierman and Steig, 1996; Savi et al., 2014; Brardinoni et al., 2020), particularly if samples are collected in small basins (Yanites et al., 2009; Marc et al., 2019). Accordingly, erosion rate estimates for basins where the sediment production has largely been controlled by landslides requires a sampling strategy where the corresponding upstream size of the basin increases with landslide area if the goal is to capture a stable long-term erosion rate signal (Niemi et al., 2005; West et al., 2014). This is also the main reason why few studies have targeted small catchments with stochastic sediment delivery (Niemi et al., 2005; Kober et al., 2012). Nonetheless, recent work (DiBiase, 2018) has demonstrated that landslides primarily introduce some scatter, but not a strong bias into erosion rate estimates. Furthermore, the use of paired cosmogenic isotopes with different half-lives, such as ^{10}Be – ^{26}Al (Wittmann and von Blanckenburg, 2009; Hippe et al., 2012; Wittmann et al., 2011) or ^{10}Be – ^{14}C (Slosson et al., 2022; Skov et al., 2019; Hippe et al., 2019; Kober et al., 2012) have enabled to reconstruct the occurrence of sediment storage in the source-to-sink sedimentary cascade. They also improved our understanding about the importance of transient erosional effects on the generation of the cosmogenic signals in fluvial material (e.g., Hippe et al., 2012).

Here, we use information offered by concentrations of cosmogenic ^{10}Be, ^{26}Al, and ^{14}C in riverine quartz, which we combine with the results of geomorphic mapping. The goal is to (i) trace the origin of the sediments, (ii) document the influence of landsliding on the long-term sediment fluxes, and to (iii) explore the scale-dependency – in space and time – of the resulting cosmogenic signals. In contrast to most previous studies, we particularly target small basins to identify the impact of landslides on the generation of cosmogenic signals. To this end, we focus our work on the Gürbe basin situated at the northern margin of the European Alps. Erosion in this basin has been largely controlled by a large variety of erosional processes including sediment supply through deep-seated landslides (do Prado et al., 2024), thus making this basin an ideal target for our goals. We thus address our aims using the concentrations of the three cosmogenic isotopes (^{10}Be, ^{26}Al, and ^{14}C) in quartz minerals, which we extracted from detrital sediments in the channel network of the Gürbe basin.

2 Local setting

The study area, the 12 km^2-large Gürbe catchment, is situated at the northern margin of the Swiss Alps (Fig. 1a). The Gürbe River, with a ~8 km-long main channel, originates at an elevation of approximately 1800 m a.s.l. There the landscape is characterised by steep cliffs made up of Mesozoic limestones that are part of the Penninic Klippen belt (Jäckle, 2013) (Fig.1b). These units are partially covered by a several meter-thick layer of glacial deposits (i.e. till, Swisstopo, 2024a). The orientation of the corresponding moraine ridges suggest deposition by small, local glaciers during the Last Glacial Maximum (LGM) ca. 20'000 years ago (Bini et al., 2009; Ivy-Ochs et al., 2022). The headwater area of the Gürbe catchment hosts a second main tributary, the Schwändligraben River (Fig. 1a). It originates within Cretaceous to Eocene Gurnigel-Flysch units, which are alternations of marls, sandstones, polymictic conglomerates and mudstones (Winkler, 1984). The landscape in the source area of this tributary is characterised by a swampy terrain and ancient deep-seated gravitational slope failures. At approximately 1200 m a.s.l., a knickzone that corresponds to the highest glacial deposits of the LGM Aare-glacier in this region (Bini et al., 2009) separates the landscape into an upper and a lower zone. At this knickzone, the longitudinal profile of the Gürbe River steepens from originally 6.5° upstream of this knickzone to 9.3° farther downstream (Fig. 1c). Similarly to the region upstream of the knickzone, the bedrock in the lower part of the Gürbe basin is predominantly composed of alternated sandstone and mudstone beds that either occur in the Gurnigel-Flysch unit (Swisstopo, 2024a) or in the Lower Marine Molasse (Diem, 1986). In this lower part of the Gürbe basin, the hillslopes are between 20° and 25° steep and covered by a dense forest made up of spruce.

Several areas prone for the occurrence of deep-seated landslides have been identified in the lower part of the Gürbe basin (Zimmermann et al., 2016). Most of them have been inactive for several tens of years (Zimmermann et al., 2016). During these times, sediment has mainly been generated through a combination of overland flow erosion and incision by small torrents that are perched on these landslides. Yet, all of these landslides have also been re-activated periodically, though not simultaneously. During such periods lasting several days up to several months, they have experienced high slip rates of several meters per day (Zimmermann et al., 2016). This has resulted in a major re-mobilization of mass also during the following years when the

landslides have become inactive. Notably, most of the active landslides are not directly connected to the main Gürbe channel
100 (Figs. 2, 3d, e). Therefore, the delivery of material from these landslides to the trunk stream occurred primarily via lateral tributaries. In cases where such deep-seated mass movements do reach the Gürbe River, undercutting by fluvial processes has triggered secondary shallow-seated landslides at their toes, resulting in material from the large landslides being directly supplied to the trunk stream. The combined effect of the aforementioned processes is a relatively high mean annual sediment discharge of c. 900 – 2600 m^3/a at the downstream end of the Gürbe basin (Zimmermann et al., 2016; do Prado et al., 2024).

105 This was the main reason why approximately 140 check dams have been built during the past century to stabilise the streambed, reduce the gradient, and thereby regulate the transport of bedload (Salvisberg, 2017; do Prado et al., 2024). At the downstream end of the lower section, the Gürbe channel transitions into the deposition zone, forming an approximately 4 km^2 alluvial fan with a distinct apex situated at 800 m a.s.l. On this fan and farther downstream, the Gürbe River flows in an artificial channel that is stabilised by check dams and flood protection dikes. After passing through an artificial deposition area, the river enters

110 the Gürbe valley floodplain, where the stream flows in a confined channel until merging with the Aare River approximately 20 km downstream.

The runoff conditions of the Gürbe River are characteristic for a pre-alpine environment, exhibiting a nivo-pluvial discharge regime (Salvisberg, 2017; Jäckle, 2013). Between 1981 to 2010 the discharge of the Gürbe River has been continuously measured at the Burgistein gauging station that is situated ca. 5 km downstream of the Grübe fan (Fig. 1a). During this period,

115 the mean annual precipitation rates have ranged from approximately 1100 mm/year in the alluvial fan area to nearly 2000 mm/year in the headwaters of the catchment (Frei et al., 2018; based on MeteoSwiss, 2014). Due to the low water storage capacity of the soils, including the soils in the Penninic Klippen belt and the regolith cover of the highly saturated, low-permeability Gurnigel Flysch and Lower Marine Molasse units, the catchment rapidly responds to high rainfall rates, resulting in peak floods with short durations (Ramirez et al., 2022). The gauging records indeed show that intense summer

120 thunderstorms, with rainfall intensities up to 30 mm/h, tend to generate runoff with large discharge magnitudes. Such an event with an extremely high discharge of 84 m^3/s occurred on the 29th of July 1990 (Ramirez et al., 2022; do Prado et al., 2024). In contrast, the mean annual discharge has been approximately 1.3 m^3/s during the survey period. These high discharge variabilities emphasise the torrential character of the Gürbe River (Ramirez et al., 2022; Salvisberg, 2022).
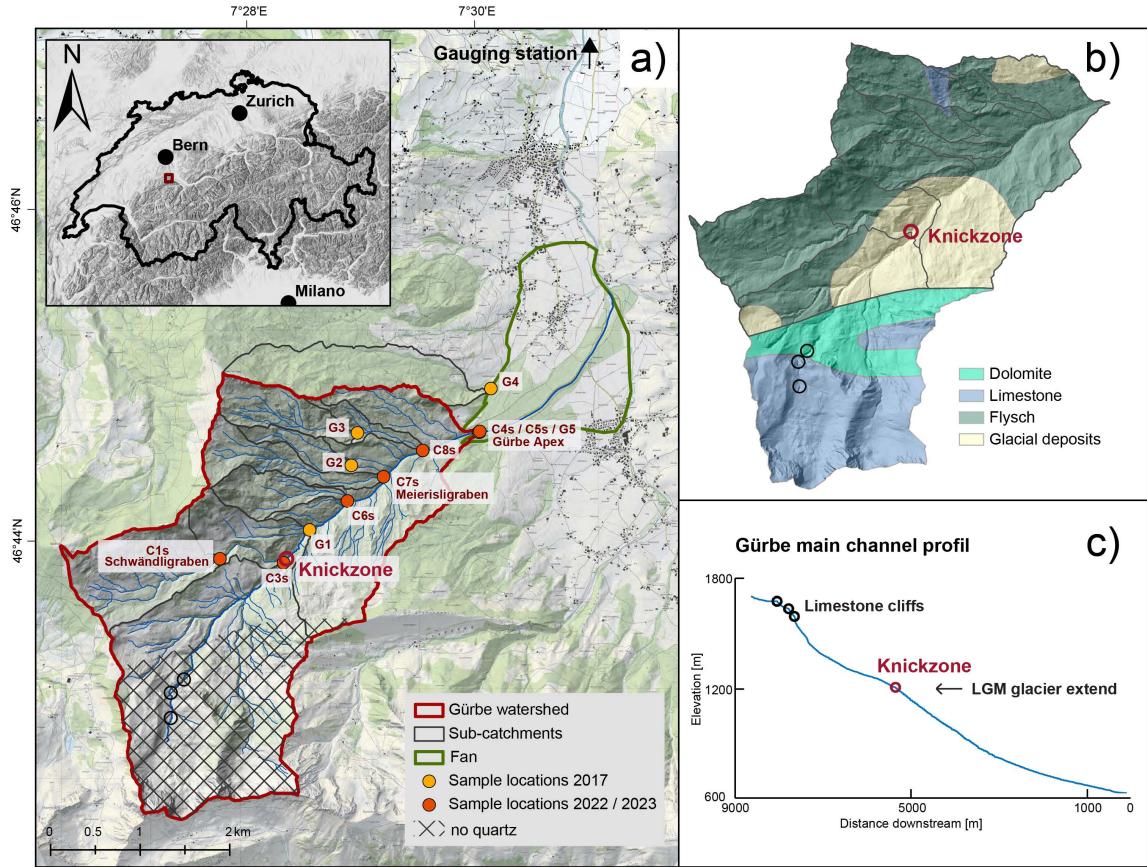
Figure 1: Overview of the Gürbe watershed. (a) Study site showing the locations where cosmogenic samples were taken during the two sampling periods in 2017 (Latif, 2019) and 2022 / 2023. The figure also illustrates the corresponding sub-catchments. The no-quartz area, which is due to the predominant occurrence of limestone lithologies, was excluded from the calculations of the denudation rates and the morphometric properties; (b) simplified lithological map, and (c) longitudinal profile of the Gürbe main channel. Note that the occurrence of knickpoints is indicated by circles. The knickzone, situated at c. 1200 m a.s.l., corresponds to the height of the LGM glacier in this region (red circle). It marks the transition from the upper to the lower part of the catchment. Further knickzones in the upper part (black circles) are conditioned by differences in the lithologic architecture of the bedrock. The digital elevation model (DEM) is taken from the Federal Office of Topography swisstopo (Swisstopo, 2024d), and the overview map showing the relief is available from Swisstopo (Bundesamt für Landestopografie swisstopo et al., 2023).

3 Methods

Following the scope of the paper, we integrated geomorphic and geologic data with cosmogenic nuclide-derived estimations of catchment-averaged denudation rates to yield a holistic picture on the origin of the sedimentary material and the source-to-sink sedimentary cascade of the clastic detritus. We used the swissAlti3D high-resolution digital elevation model (DEM; Swisstopo, 2024d) with a spatial resolution of 2 m as a basis, which we then re-sampled (with the nearest neighbour algorithm) to a 5 m-DEM for further scaling analysis. We justify this re-sampling to a lower resolution because a grid with a lower

140 resolution prevents the introduction of artefacts upon calculating the flow paths (such as roads, and artificial scours). Additionally we corrected the DEM of the Meierisligraben catchment (Fig. 1) to account for the re-direction of the corresponding channel during the reactivation of the corresponding landslide in 2018, a feature already documented in the swisstopo map 1:10'000 (Swiss Map Raster 10; Swisstopo, 2024c). This correction was performed by digitizing a new DEM using the contour lines of the respective map as a basis. Next, we used the natural neighbour interpolation method (Sibson,

145 1981) as implemented in ArcGIS Pro v3.1 to create a raster dataset from the contour lines. The corrected area was then integrated into the 5 m-DEM. We used this updated topographic model for (i) the quantification of the morphometric properties of the study area contributing to the generation of cosmogenic isotopes (area that supplies quartz, see section 3.1), (ii) the establishment of a geomorphic map illustrating the erosional processes within the Gürbe basin, and (iii) the calculation of the catchment-averaged denudation rates from the measured concentrations of the cosmogenic isotopes ^{10}Be, ^{26}Al and ^{14}C.

150 **3.1 Morphometric characterisation**

We delineated the different sub-catchment areas in ArcGISPro (v3.1) using the 5 m-DEM as a basis (see previous section). In addition, we computed the sediment connectivity index with the algorithm developed by Borselli et al. (2008) and adapted for alpine catchments by Cavalli et al. (2013). The related algorithm is implemented as an ArcGIS toolbox in ArcMap (v.10.3.1), which we employed accordingly for our study. The sediment connectivity index is based on topographic data and designed to

155 represent the physical connectivity between different areas within an alpine catchment. It thus expresses the probability for sediment, originating in a specific location on a hillslope, to reach the defined targets, such as the main channel or the outlet of a catchment. For the details on the computation we refer to the sections 2.1 and 2.2 in Cavalli et al. (2013) where the corresponding equations 1 to 5 are presented.

A compilation of geologic data includes the collection of information on quartz-bearing lithologies, the occurrence of glacial

160 deposits and the extent of the LGM. We gathered such data from three map datasets including i) the GeoCover (Swisstopo, 2024a) based on Heinz et al. (2023) and Tercier and Bieri (1961), ii) the Geological Map of Switzerland 1:500'000, and iii) the Map of Switzerland during the Last Glacial Maximum (LGM) 1:500'000 (GeoMaps 500 Pixel; Swisstopo, 2024b). Based on this data we grouped the stratigraphic units into quartz-bearing and non-quartz-bearing lithologies (Fig. 1a). As a subsequent step, we corrected the catchment shapes for the occurrence of quartz minerals in bedrock and glacial deposits, thereby clipping

165 the areas with limestone lithologies in the upper part of the catchment where quartz is absent (Figs. 1a and 1b). For the remaining sub-catchments, which contribute to the cosmogenic signals in the channel network because they contain quartz grains, we computed a range of routinely used topographic metrics including slope gradient, terrain ruggedness and channel steepness (e.g., Delunel et al., 2020). Slope gradient and terrain roughness were estimated using tools implemented in ArcGIS (v3.1) pro. We used the terrain ruggedness index (TRI) by Riley et al. (1999) to quantify local terrain variability. This was

170 done by calculating the mean elevation difference between each grid cell and its eight neighbouring cells.

The extraction of river profiles, the calculation of the normalised channel steepness index (k_{sn}) and the mapping of knickpoints was accomplished with the corresponding tools of Topotoolbox (v2.2, Schwanghart and Scherler, 2014). For these calculations,

we considered stream segments that have an upstream drainage area >2000 pixels, and that contribute to the generation of detrital quartz grains. In addition, k_{sn} values were calculated for each cell of the stream network, and then averaged over 125 m-long channel segments, thereby employing a k_{sn}-radius of 500 m. This corresponds to a threshold area of 1000 m^2 and a minimum upstream accumulation area of 0.01 km^2. As reference concavity we used the default value of $\theta = 0.45$ (Schwanghart and Scherler, 2014).

3.2 Mapping

It has been shown that landsliding, channel incision and overland flow erosion (also referred to as hillslope diffusion in the modelling literature; e.g., Tucker and Slingerland, 1997) are the most important erosional mechanisms contributing to the generation of sediment in a pre-Alpine catchment (Battista et al., 2020). Accordingly, we created an inventory of such processes and potential sediment sources using a variety of methods and data sources. We reconstructed the spatial distribution of landslides through (i) a compilation of already published maps, (ii) an analysis of information available from historical orthophotos, and (iii) observations in the field. Here, we used the landslide inventory from the Natural Hazards Event Catalogue referred to as Naturereigniskataster (NGKAT, 2024) as a basis, which is available from the 'Geoportal des Kantons Bern'. We updated this database with information that we retrieved upon analysing historical orthophotos. In this context, the black and white orthophotomosaic images cover the time interval between 1946 and 1998 (SWISSIMAGE HIST; Swisstopo, 2024f). In addition, the time span between 1998 to the present is represented by the three consecutive orthophotomosaics. These latter images have a better spatial resolution than the previous ones (SWISSIMAGE 10 cm; Swisstopo, 2024e). We used these images as a basis to reconstruct the occurrence of topographic changes in the Gürbe catchment over multiple decades. We complemented this dataset with observations on the hillshade DEM, and the maps displaying the slopes and terrain roughness index (TRI) to complete the inventory of landslide occurrence in the study area. We additionally aimed at distinguishing between shallow landslides and thus surficial processes, and deep-seated movements. Shallow landslides, typically covering areas of a few square meters, were identified based on the occurrence of (i) erosion scars resulting in surfaces that are free of vegetation, (ii) small scale depressions in the head of the inferred landslides ('Nackentälchen' according to Haldimann et al., 2017), and (iii) regions characterised by a down-slope increase of the hillslope angle because an escarpment, characterizing the head of a landslide, is typically steeper than the stable area farther upslope (visible in the slope and TRI, see also Schlunegger and Garefalakis, 2023). In contrast, the deep-seated landslides that cover larger areas are characterised by the occurrence of (i) potentially vegetation free areas, (ii) altered vegetation such as sparse or smaller trees with a light colour on the satellite imageries, and (iii) zones of slip that are marked by sharp edges separating a smooth topography above the escarpment edge from an uneven, bumpy terrain below it. Upon mapping landslides, we paid special attention to recognise whether such sediment sources are connected with the channel network, thereby contributing to the bulk sedimentary budget of the Gürbe River.

Incised areas are generally characterised by a V-shaped cross-sectional geometry (Battista et al., 2020). Accordingly, we mapped the upper boundary of such a domain where the landscape is characterised by a distinct break-in-slope. There, the

landscape abruptly changes from a gentle morphology above this edge to a steep terrain farther downslope (e.g., Fig. 2C in Cruz Nunes et al., 2015). The steep slopes ending in a channel forming such incisions usually expose the bedrock or the non-consolidated material into which the incision has occurred. Similar to the approach of van den Berg et al. (2012) and Battista et al. (2020), we used the aforementioned criteria to identify such incised areas on the DEM and in the field. Furthermore, we mapped areas where sediment generation has been accomplished through overland flow erosion. In a landscape, such segments are characterised by gentle slopes and smooth transitions between steep and flat areas. They can be readily identified on a hillshade-DEM by their smooth surface texture, lacking evidence for the occurrence of bumps, hollows and scars (Battista et al., 2020; van den Berg et al., 2012). Finally, we also mapped the occurrence of scree deposits (Savi et al., 2015), which occur locally at the base of limestone cliffs. All information were assembled and synthesised in an ArcGIS environment to produce a geomorphic map, illustrating the areas of landslide occurrence.

3.3 Catchment-wide denudation rates inferred from concentrations of cosmogenic ^{10}Be, ^{26}Al and ^{14}C

3.3.1 Sampling strategy and data compilation

During autumn 2022 and spring 2023 we collected a total of seven riverine sand samples at six locations for the analysis of the cosmogenic nuclides ^{10}Be, ^{26}Al and ^{14}C. Each sample consisted of 2–4 kg of sand taken from the active channel bed. We sampled material at those sites where we anticipate capturing the different source signals that result from the various erosional mechanisms (overland flow erosion, incision, and landsliding, see section 3.2). Accordingly, the uppermost sample (C1s) is taken in the Schwändligraben River, which is the main upstream tributary (Fig. 1a). Mapping suggests that at this site the concentration of the cosmogenic isotopes will characterise the signal related to overland flow erosion. A second sample (C3s) was collected in the Gürbe stream just upstream of the confluence with the Schwändligraben River. Similarly to sample C1s, the riverine material taken at site C3s is expected to record a cosmogenic signal related to overland flow erosion, yet it is expected to partially also record the contribution of material derived from the incised area (see section 3.2). We then sampled material from three tributaries draining the area with the deep-seated landslides on the NW orographic left side (samples C6s, C7s and C8s). Finally, we collected two sand samples at the outlet of the catchment and thus at the Gürbe fan apex (C4s and C5s), where the stream starts to flow on the fan. Here, the goal is to characterise the cosmogenic signal representing the mixture of the supplied material from farther upstream. We took one sand sample from the gravel bar close to the active channel and another one from a gravel bar that is situated on the left lateral margin of the Gürbe channel. Upon sampling, we anticipated that fluvial reworking on this second bar – due to its lateral position – has occurred less frequently than material transport in the active channel. In addition, these two separate samples were collected to evaluate the consistency of the mixed sediment signal at the outlet of the catchment.

We also included ^{10}Be concentrations of 5 samples (G1 to G5) collected in 2017 and presented in Delunel et al. (2020) and Latif (2019) in our analysis (Fig. 1a). Site G1 is situated ca. 500 m downstream of the confluence between the Gürbe and Schwändligraben rivers and downstream of the incised area. Accordingly, we anticipate that the ^{10}Be concentration of the

riverine sand from this site carries the erosional signal related to the combined effect of overland flow erosion and fluvial incision (van den Berg et al., 2012; Battista et al., 2020). Sites G2 and G3 are located in tributary channels on the orographic left side where sediment has been derived from the landslides. Similarly, to sites C6s to C8s, we expect the concentrations at these sites to characterise the cosmogenic signals related to a material supply from the deep-seated landslides. Site G5 is located on the Gürbe fan apex and is expected to capture the erosional signal of the entire Gürbe catchment. Finally, site G4 is situated in a neighbouring river, which collects the sedimentary material from a drainage basin that is perched on a deep-seated landslide adjacent to the Gürbe catchment farther to the North. We included the ^{10}Be concentration from site G4 in our study because surface erosion in this catchment is not conditioned by the processes of the Gürbe River, thus yielding an independent constrain on denudation occurring in an area where deep-seated landslides have shaped the landscape and contributed to the generation of detrital material.

3.3.1 Laboratory work

The sand samples were sieved to isolate the 250 – 400 µm grain size fraction. However, due to insufficient material in this size range, the 400 µm – 2 mm sand fraction was subsequently crushed and re-sieved to obtain sufficient material with the desired grain size. Further sample processing was performed according to the protocols originally reported in Akçar et al. (2017). The 250 – 400 µm fraction underwent magnetic separation as a preliminary step, followed by the removal of carbonate minerals trough HCL and successive leaching treatments using hydrofluoric acid, phosphoric acid, and aqua regia to purify the quartz. After measuring the total Al content, additional leaching was performed to further reduce impurities and lower the total Al concentrations. Approximately 40 g of purified quartz was spiked with the ^{9}Be carrier BL-SCH-3 and dissolved in concentrated hydrofluoric acid. Be and Al were stepwise extracted from this solution using anion and cation exchange chromatography, thereby following the protocol of Akçar et al. (2017). The extracted and precipitated Be and Al isotopes were oxidised and pressed into targets for the subsequent measurements of the ^{10}Be/^{9}Be and the ^{26}Al/^{27}Al ratios with the accelerator mass spectrometry (AMS) MILEA facility at the ETH Zürich (Maxeiner et al., 2019). The measured ^{10}Be/^{9}Be ratios were normalised with the ETH in-house standard S2007N (Kubik and Christl, 2010) and corrected using a full process blank ratio of 3.92 ± 1.07 x 10^{-15}. The measured ^{26}Al/^{27}Al ratios were normalised to the ETH AMS standard ZAL02N (equivalent to KNSTD, Kubik and Christl, 2010; Christl et al., 2013) and corrected for a small constant background rate. Total Al concentrations, which we measured with the ICP-MS in the aliquot taken from each sample solution, are used to calculate ^{26}Al concentrations from the isotope ratio.

For six samples (C1s, and C3s to C7s) three to four grams of the purified quartz were further processed at the ETH facility for measuring the concentrations of the in-situ ^{14}C (Lupker et al., 2019). The extraction of this isotope was performed following the updated protocol of Hippe et al. (2013). Accordingly, we heated the cleaned quartz in a degassed platinum crucible under ultra-high-purity oxygen to remove contaminants. The ^{14}C isotopes were then extracted by heating the sample to 1650°C in two cycles for 2 hours each, with an intermediate 30 minutes-long heating step at 1000°C. The extraction was performed under static O_2 pressure in the oven. At the end of the extraction line, the purified CO_2 was trapped and flame sealed using LN. The

released gas was purified using cryogenic traps and a 550°C Cu wool oven, and the amount of pure CO_2 was measured manometrically before being prepared for the subsequent AMS analysis. CO_2 samples were analysed using the MICADAS 200 kV AMS instrument with a gas ion source at the ETH/PSI, which enables the measurement of small carbon samples (2–100 µg C) without requiring graphitization (Synal et al., 2007). The reduction of the AMS data followed the protocols outlined by Hippe et al. (2013) and Hippe and Lifton (2014).

3.3.3 Calculation of denudation rates

We calculated catchment wide denudation rates using the online erosion rate tool formerly known as the CRONUS-Earth calculator (v3, Balco et al., 2008), employing a time independent production scaling (Lal, 1991; Stone, 2000). For the bedrock density, we utilised the widely used value of 2.65 g/cm³. We corrected the scaling calculations for quartz-free regions by using centerpoints and mean catchment elevation derived for only the area that is made up of quartz-bearing lithologies (see above). Following recommendations of DiBiase (2018), no correction for topographic shielding was applied. As shielding due to temporary snow cover leads to a decrease of in-situ cosmogenic nuclide production rates for ^{26}Al and ^{10}Be (e.g., Delunel et al., 2014), we applied a snow cover shielding factor using the empirical approach of Delunel et al. (2020), which itself is based on Jonas et al. (2009). Therein, snow shielding factors were determined as a function of the catchment's mean elevation.

The erosion rates inferred from cosmogenic nuclides are frequently used to estimate the time needed to erode the uppermost 60 cm of material under the assumption of steady state denudation, which is referred to as integration time (Bierman and Steig, 1996; Granger et al., 1996). However, due to landslide perturbations we instead calculated the minimum exposure age as a proxy for the integration time. We thus calculated such time spans for all our nuclide-derived denudation rates, using the same online calculator under the assumption of no erosion and no inheritance.

3.4 Whole-rock geochemical analysis

In order to determine how the supply of sediment from various sources influences the overall sedimentary budget of the Gürbe catchment and the composition of the material in the channel network, we proceeded in a similar way as Glaus et al. (2019), Stutenbecker et al. (2018) and Da Silva Guimarães et al. (2021), measuring the whole rock composition of seven samples (C1s, C3s – C8s). The whole rock geochemical analysis was performed by Actlabs in Canada on sample material before separating the magnetic constituents (see section 3.3.1 above) with grain size < 250µm. Elements and major oxides were measured in lithium borate fusion glasses through Inductively Coupled Plasma Mass Spectrometry (ICP-MS). The analytical package included the measurements of the major element oxides: SiO_2, Al_2O_3, Fe_2O_3, MnO, MgO, CaO, Na_2O, K_2O, TiO_2, P_2O_5 as well as the trace elements Ba, Sr, Y, Sc, Zr, Be, V. Additional elements Ag, Cd, Cu, Ni, Pb, Zn, S were measured based on multiacid digestion and TD-ICP. Correction was done by the loss of ignition (LOI). We performed a principal component analysis (PCA) with the scikit learn package – implemented in Python (Pedregosa et al., 2011) – on the geochemical data with the aim to identify different source lithologies and to fingerprint potentially different sediment compositions from the individual sub-catchments.

4 Results

4.1 Mapping, inferred erosional mechanisms and morphometric characterisation

305 The mapping results allow us to distinguish between three main zones within the Gürbe catchment, which are the upper zone, the lower zone and the fan area (Figs. 1a, 2a and 2b, 3). The upper zone has predominantly been affected by small, shallow landslides (Fig. 2a). The resulting scars are visible in the historic and current orthoimages. The displaced material has in most cases no obvious connection to the drainage network. Additionally, a few scree deposits exist at the base of limestone cliffs (Fig. 2a, 3a); however, as they are not linked to the drainage network, they do not contribute to the sediment budget of the

310 river network. Overall, the landscape was smoothened by glacial and periglacial processes during the LGM, while the channel network is distinctly defined by its linear geometry (Fig. 2a, 3b). There, channel incision has resulted in the creation of sharp, yet locally constrained escarpments between the hillslopes and the riverbanks. This upper zone is also characterised by a generally low connectivity between the hillslopes and the channel network (Fig. 2c). Except for the spatially disconnected cliffs, the hillslopes are generally gentle to moderately steep (Fig 3a and 3b), displaying a mean hillslope angle of 19.2°. In

315 addition, the channel network is characterised by generally low mean normalised steepness values ranging between 26.5 $m^{-0.9}$ and 30.0 $m^{-0.9}$ for the two sub-catchments.

In the lower zone, numerous medium- to deep-seated landslides are observed (Fig. 2a, 3d and 3e). The landscape in this area is characterised by an absence of stable, deeply incised channels, with a channel network instead appearing less well developed. Apparently, the channels adjacent and perched on these landslides have been deflected multiple times during major landslide

320 events (e.g., Simpson and Schlunegger, 2003). In comparison to the upper part, the connectivity between hillslopes and the channel network is higher (Fig. 2c), the hillslopes are generally steeper (mean average hillslope angle of 21.8°), and the tributary and as well as the trunk channels have generally higher steepness values, ranging from 32.4 $m^{-0.9}$ to 43.4 $m^{-0.9}$.

The boundary between these two zones is marked by a V-shaped erosional scarp indicating the occurrence of incision (Fig. 3c). This also aligns with the occurrence of the major knickzone along the Gürbe main channel, which is situated at around

325 1200 m a.s.l and marks the transition reach from the upper to the lower zone (Figs. 1c and 2a). This knickzone reach is readily visible by the change in the steepness values of the channel network, which are higher along the incised reach than upstream and downstream of it.
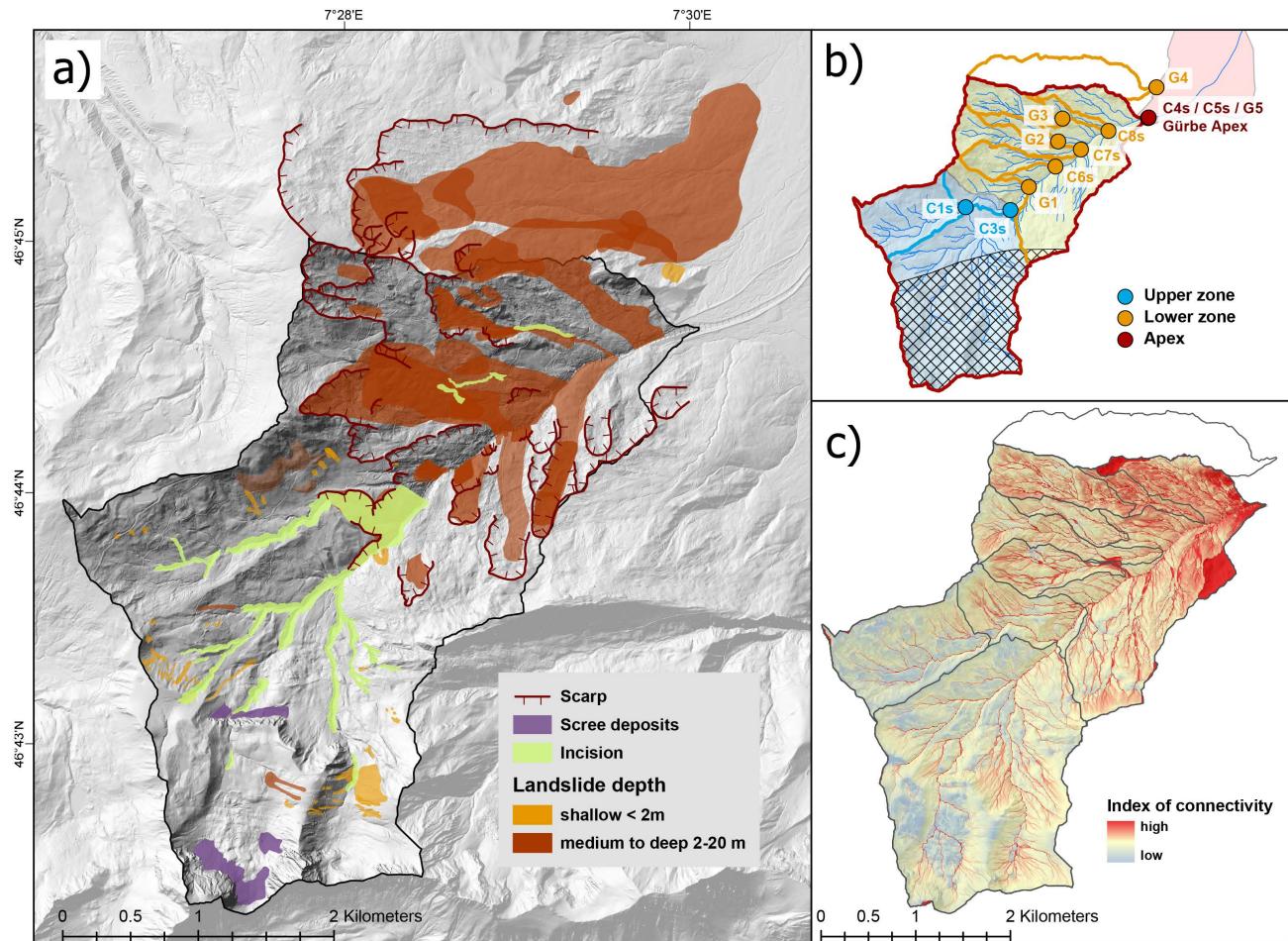
Figure 2: Geomorphic map of the Gürbe catchment. (a) Mapping indicates two distinct geomorphic zones: 1) the southern, upper part of the catchment is characterised by incised channels, limited scree deposits, and shallow landslides; 2) the northern, lower part is a dissected and topographically complex landscape marked by multiple medium- to deep-seated landslides. (b) Delineation of three zones: the upper zone (blue), the lower zone (orange), and the sampling locations at the fan apex (red), which represents the site where sediment is supplied to the depositional area. (c) Index of connectivity with respect to the fan apex. The upper zone exhibits a low connectivity between hillslopes and the channel network, while the connectivity increases markedly in the lower zone, reflecting that the pathway of sediment transfer – relative to the fan apex – is more direct for sediment originating in the lower part than in the headwater region. Digital elevation model (DEM) from the Federal Office of Topography swisstopo (Swisstopo, 2024d).
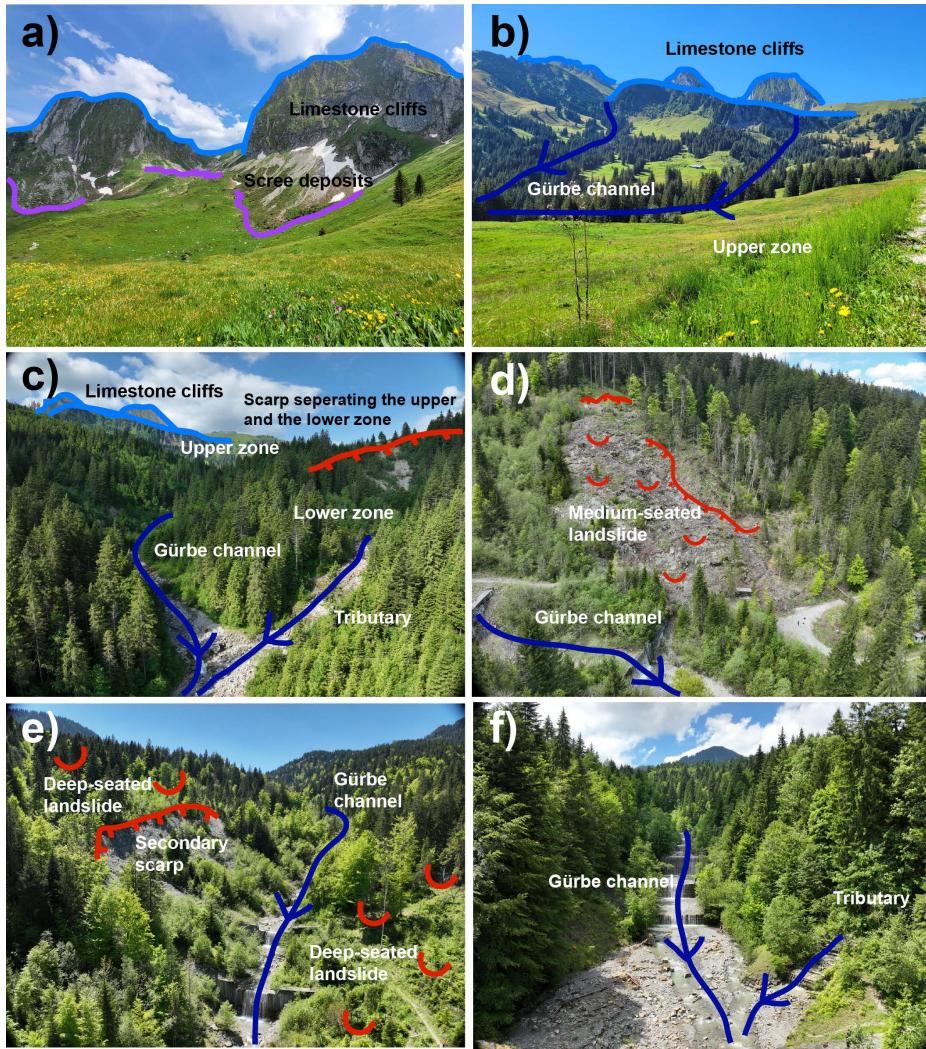
Figure 3: Drone images visualizing the catchment's characteristics. (a) Upper zone with limestone cliffs and scree deposits. (b) Upper zone with smooth landscape and the limestone cliffs. c) Knickzone area separating the upper from the lower zone. (d) and (e) Scars in the landscape along the Gürbe main channel indicating that landslides have recently been active. (f) Confluence between the Gürbe River and a tributary torrent upstream of the apex.

4.2 Cosmogenic nuclide concentrations

The ^{10}Be concentrations in all 12 samples range from the lowest value of $2.50 \pm 0.20 \times 10^4$ at/g with given 2σ uncertainties (resp. $2.19 \pm 0.25 \times 10^4$ at/g) measured in the sample G4 to the highest value of $8.67 \pm 0.48 \times 10^4$ at/g measured in the uppermost sample C1 (Table 1, S2). A comparison of the values across the catchment shows a distinct pattern across the study area. In the upper zone, characterised by sites C1s and C3s (Fig. 1a), the concentrations of in-situ ^{10}Be are up to three times higher than those measured at the outlet of the Gürbe catchment (sites C4s, C5s and G5, Fig. 1a). This pattern suggests a

significant supply of sediment with low ^{10}Be concentrations to the Gürbe channel downstream of sites C1s and C3s in addition to the effect related to the differences in the catchment's elevations. The tributaries, characterised by samples taken at sites C6s–C8s, G2 and G3 (Fig. 1a), contribute sediment with concentrations at or below those recorded at the outlet (Table 1), confirming their role as sources of material with lower concentrations. This is also the case for the low ^{10}Be concentration in sample G1 taken downstream of the knickzone, recording a signal that is caused by the large sediment input along the incised area. Additionally, among the three samples taken at the apex of the Gürbe fan, the two samples collected at different times (C4s & G5) show nearly identical ^{10}Be concentrations (3.23 ± 0.21 & $3.27 \pm 0.31 \times 10^5$ at/g). Similarly, also the third sample C5s, taken during the same survey as sample C4s but from the margin of the active channel bed, displays a ^{10}Be concentration that is nearly the same (within uncertainties) as the concentrations measured for the two samples from the same location.

The measured ^{26}Al concentrations show a pattern that is similar to that of ^{10}Be across the catchment. The lowest concentration ($19.38 \pm 2.18 \times 10^4$ at/g) is recorded in the sample that has also the lowest ^{10}Be value, while the highest ^{26}Al concentration ($64.21 \pm 4.85 \times 10^4$ at/g) was measured in the same sample that has also the lowest ^{10}Be concentration (material taken from the uppermost site in the catchment; Table 1, S3). At the Gürbe fan apex, the two samples collected at different locations show no statistically significant differences in their ^{26}Al concentrations ($24.07 \pm 2.80 \times 10^4$ at/g for sample C4s versus $22.65 \pm 2.18 \times 10^4$ at/g for sample C5s).

The ^{14}C concentrations of the six sediment samples (C1s, C3s to C7s) range from $3.47 \pm 0.21 \times 10^4$ at/g to $11.50 \pm 0.46 \times 10^4$ at/g (Table 1, S5). While the lowest and highest concentrations are consistently recorded in the same two samples (C7s for the lowest and C1s for the highest concentration), the in-situ ^{14}C concentrations of the other samples display different spatial patterns than the other nuclides. Additionally, the concentrations measured in the two samples at the fan apex significantly differ from each other.

The ^{26}Al/^{10}Be ratios range from 6.27 and 9.54 and, within a 2σ uncertainty. The highest ratios of >7.76 are observed in the three tributaries. The ratios of ^{10}Be/^{14}C range between 0.40 and 0.75.

Table 1: Measured [10]Be, [26]Al and ^{14}C concentrations for all samples. All uncertainties given are 2σ standard deviation and include the statistical uncertainties of the AMS measurement, the blank error (for [10]Be) and the uncertainties of the ICP-MS measurements (for [26]Al). The respective zone where the sample was taken is indicated in the column Z with 1 for the upper zone, 2 for the lower zone and 3 for the Apex.

Samp.	Z	Lat. [°]	Long. [°]	Alt. [m.a.s.l.]	^{10}Be Concentration [10^4 at/g]			^{26}Al Concentration [10^4 at/g]			^{14}C Concentration [10^4 at/g]			^{26}Al/^{10}Be			^{10}Be/^{14}C		
C1s	1	46.73025	7.46171	1359	8.67	±	0.48	64.21	±	4.85	11.50	±	0.46	7.41	±	0.69	0.75	±	0.05
C3s	1	46.72989	7.47103	1214.1	4.81	±	0.29	34.79	±	2.46	6.88	±	0.58	7.23	±	0.67	0.70	±	0.07
C4s	3	46.7431	7.4998	765.6	3.23	±	0.21	24.07	±	2.80	7.07	±	0.28	7.44	±	0.99	0.46	±	0.04
C5s	3	46.74296	7.49982	765.6	3.61	±	0.23	22.65	±	2.18	5.10	±	0.41	6.27	±	0.72	0.71	±	0.07
C6s	2	46.73607	7.4804	1022.1	2.92	±	0.20	25.71	±	3.30	7.27	±	0.29	8.81	±	1.28	0.40	±	0.03
C7s	2	46.73847	7.48562	927.2	2.50	±	0.20	19.38	±	2.18	3.47	±	0.21	7.76	±	1.07	0.72	±	0.07
C8s	2	46.74119	7.49132	842.8	3.21	±	0.21	30.62	±	3.17				9.54	±	1.17			
G1	2	46.73314	7.474846	1126.3	3.42	±	0.34												
G2	2	46.739704	7.481027	1042.3	3.20	±	0.28												
G3	2	46.742879	7.481919	1025.1	3.14	±	0.31												
G4		46.747332	7.501382	724.3	2.19	±	0.25												
G5	3	46.743069	7.499663	766.2	3.27	±	0.31												

4.3 Denudation rates

The erosion rates calculated for the three different nuclides are presented in Figures 4 and 5 (full data available in Table S6 in the Supplement) against the upstream distance of the sampling location relative to the Gürbe fan apex. In general, the [10]Be-
380 derived erosion rates range from 0.1 mm/yr to 0.3 mm/yr in one of the tributaries. Upstream of the knickzone, the [10]Be-based erosion rates are below 0.2 mm/yr, while downstream of the knickzone, the erosion rates increase to values between 0.2 mm/yr and 0.3 mm/yr. A comparison between [10]Be- and [26]Al-derived erosion rates shows that the rates are the same within uncertainties in the upper catchment, but they differ in the tributaries downstream of the knickzone and at the fan apex. Specifically, [26]Al-derived erosion rates are higher than the corresponding [10]Be-derived rates at the Gürbe fan apex, whereas in
385 the tributaries they are lower. The ^{14}C-derived erosion rates range from 0.2 mm/yr to 1.0 mm/yr. They are thus up two to three times higher than those derived from the other longer-lived nuclides. The differences Δε between the calculated denudation rates (Fig. 4) range from 0.005 mm/yr up to 0.06 mm/yr (Δε between [26]Al- and [10]Be-based rates), and from 0.08 mm/yr up to 0.64 mm/yr (Δε between [14]C- and [10]Be-based rates).

The denudation rates presented above can be used to estimate the timespan over which the cosmogenic data have integrated
390 the erosional processes, which in our case, is approximately 3'000 to 6'000 years. More specifically, in a zero-erosion scenario, the minimum duration of exposure required to accumulate the measured [10]Be and [26]Al concentrations ranges from 2'000 to 6'000 years, while for ^{14}C concentrations it ranges from 800 to 3'000 years (Table S6).
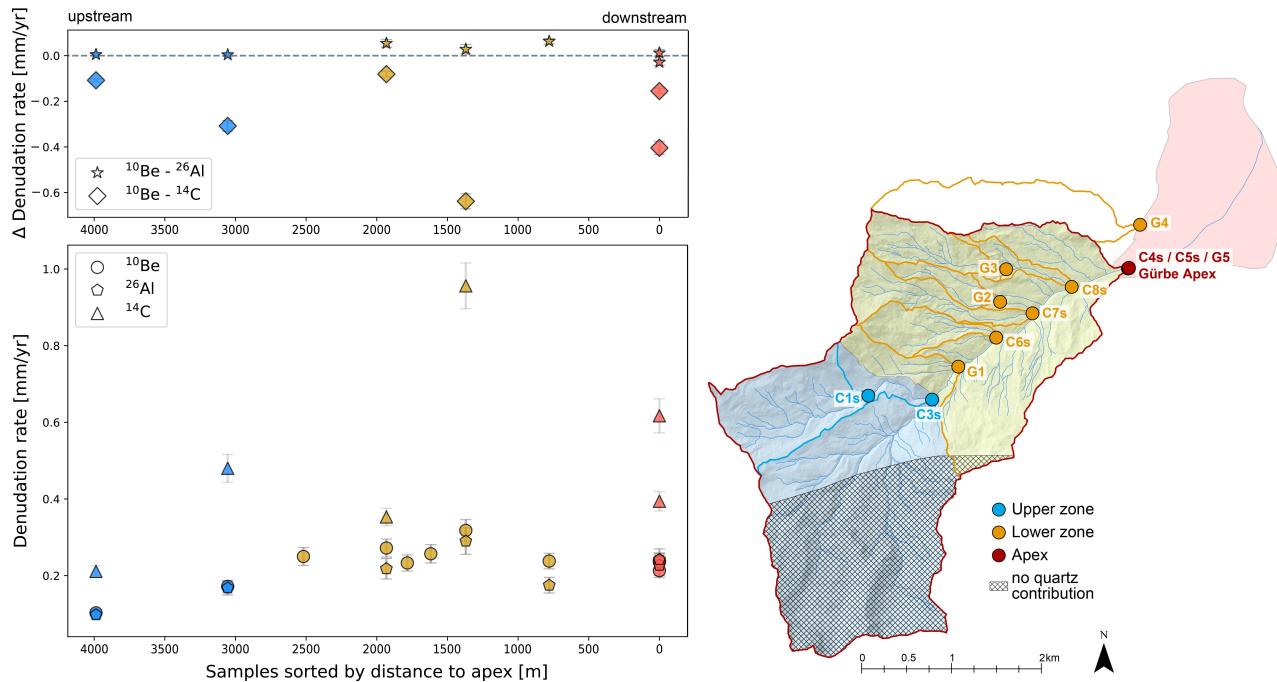
395 **Figure 4: Denudation rates calculated based on the measured ¹⁰Be, ²⁶Al and ¹⁴C concentrations.** Each colour indicates the zone represented by the corresponding samples, with blue characterizing the upper zone, yellow the lower zone, and red the Gürbe fan apex. The digital elevation model (DEM) is taken from the Federal Office of Topography swisstopo (Swisstopo, 2024d).
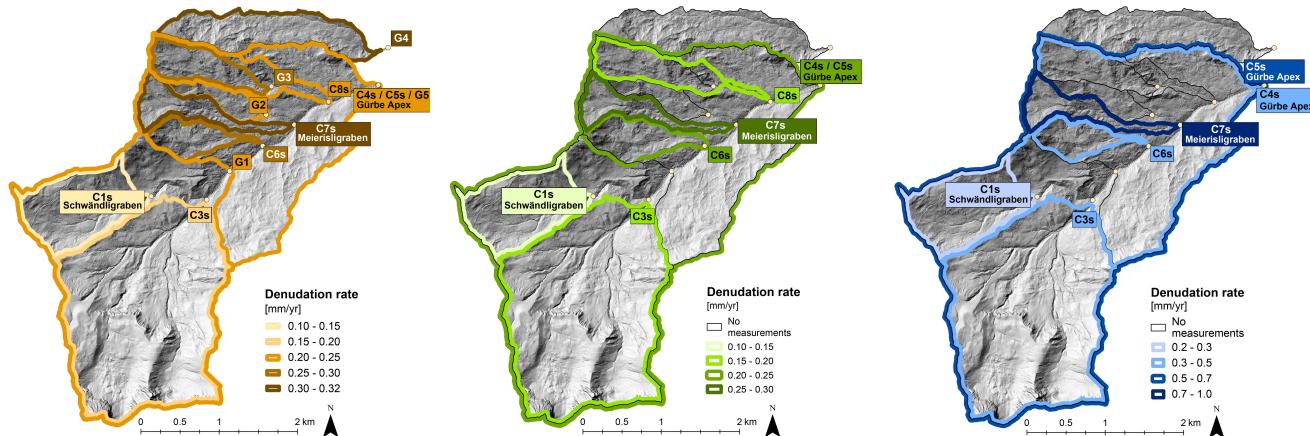
Figure 5: Denudation rates calculated based on the ¹⁰Be (left), ²⁶Al (middle) and ¹⁴C (right) concentrations. The lighter colours
400 illustrate the highest concentrations (measured in the sample C1s representing the Schwändligraben sub-catchment in the upper zone). The lowest nuclide concentrations were measured in sample C7s, representing the Meierisligraben tributary in the lower zone. The digital elevation model (DEM) is taken from the Federal Office of Topography swisstopo (Swisstopo, 2024d).

4.4 Geochemical composition of sediment

405 The analysed samples showed variable SiO_2 contents (33 -58 %-wt) and Al_2O_3 (5 – 12 %-wt), which are anticorrelated with CaO concentrations (8% to 29%; Table S6). Here, the samples from catchments with limestone-bearing lithologies (e.g. C3s; Fig.2) show the highest concentrations of CaO and the lowest ones of SiO_2 and Al_2O_3 (Table S6), resulting in a pattern where the CaO concentrations decrease in the downstream direction. This reflects the corresponding trend in exposed lithologies where the relative proportion of limestones in the basin decreases downstream. The relative abundance of all other major

410 oxides varies significantly between individual samples (Table S6). Similarly, the concentrations of the trace elements did not vary strongly, with the main trace elements being Sr (325 ppm to 717 ppm), Ba (140 ppm to 310 ppm) and Zr (90 ppm to 220 ppm). Apart from the downstream-decreasing trend of geochemical signals associated with limestone lithologies (Penninic Klippen Belt) – relative to those indicative of SiO_2- and Al_2O_3-rich bedrock (Flysch and Molasse units) – no systematic variation in geochemical composition is observed, either for the major oxides or for the trace elements (Supplementary Fig.

415 S1).

5 Discussion

The concentrations of the cosmogenic isotopes ^{10}Be and ^{26}Al and the resulting erosion rates show distinct differences between the upper, gently sloping region and the lower, steeper zone of the catchment (Figs. 4 and 5). We first discuss the implications of this pattern and particularly explore how the cosmogenic signals within the Gürbe basin change in the downstream direction as sediments derived from landslides impact the cosmogenic signal towards the catchment's outlet near the fan apex (section 5.1). Next, we combine the ^{10}Be, ^{26}Al, and ^{14}C datasets to investigate the erosional dynamics across different temporal scales. By comparing the signals preserved by these isotopes, we assess whether the cosmogenic nuclide concentrations reflect the occurrence of steady erosion over varying timescales, or if they record the effects of inheritance, burial, or transient perturbations over the same timescales (sections 5.2 and 5.3). As a next aspect, we discuss (i) how the cosmogenic nuclide-based erosion rates relate to the landscape's architecture by comparing them with the mapping results (section 5.4), and (ii) how this pattern has been conditioned by the glacial carving during the past glaciations (section 5.5). We end the discussion with a notion that in drainage basins where the bedrock is too homogeneous to pinpoint the origin of the detrital material, terrestrial cosmogenic nuclides offer a viable tool for provenance tracing (section 5.6).

5.1 Downstream propagation and scale dependency of cosmogenic signals

The ^{10}Be and ^{26}Al concentrations, and consequently the inferred denudation rates, record the occurrence of a variety of erosional mechanisms across the Gürbe basin. In the upper part of the catchment, high cosmogenic nuclide concentrations correspond to low denudation rates. This contrasts with the lower nuclide concentrations and higher erosion rates inferred for the samples collected in the tributaries of the lower zone, along the incised reach downstream of the knickzone (sample G1), and at the fan apex (Fig. 6). This downstream decrease in concentrations of both nuclides suggests that the pattern of sediment generation has been stable over the erosional timescale recorded by them. Such an interpretation is corroborated by the same nuclide concentrations (within uncertainties) encountered in the three riverine samples at the fan apex. This is surprising because sediment supply through landsliding – in our case in the lower zone – introduces a stochastic variability into the generation of sediment. Such a mechanism was already demonstrated for other Alpine torrents (Kober et al., 2012; Savi et al., 2014), where stochastic processes such as landslides and debris flows have resulted in episodic supply of sediment with low ^{10}Be concentrations (Niemi et al., 2005; Kober et al., 2012). This has the potential to perturb the overall cosmogenic signal particularly in small catchments (Yanites et al., 2009; Marc et al., 2019), thereby (i) leading to variations in nuclide concentrations within riverine sediments collected from the same channel bed (Binnie et al., 2006) and (ii) introducing scatter into the dataset (DiBiase et al., 2023). Given the small area (12 km^2) and the prevalence of recurrent landslides in the Gürbe sub-catchments, one might expect the sedimentary material at the Gürbe fan apex to record such variations. Yet our results indicate that the overall denudation signal has remained nearly stable at the fan apex (Fig. 6). This highlights an important scale-dependency in the erosional controls governing the generation of cosmogenic signals in the Gürbe basin. In particular, at smaller spatial scales (0.25 – 3.5 km^2), denudation rates reflect the controls of local geomorphic and geologic conditions on

erosion and material supply, such as repeated deep-seated landsliding as in the case presented here. However, when these
450 signals with a local origin are aggregated downstream towards the fan apex, they are recorded as a mixed, more stable signal that averages out the high and low concentrations generated in the individual sub-catchments. In the Gürbe basin, such mixing appears to occur at a spatial scale of less than 10 km². We thus infer – as this has already been mentioned by the many studies referred to in this paper in previous sections – that cosmogenic nuclides remain a suitable tool for estimating long-term average erosion rates over thousands of years for landscapes that have been eroded at rates between 0.1 and < 1 mm/yr (von
455 Blanckenburg, 2005). This holds true even for catchments influenced by repeated stochastic processes – such as those documented for landslide processes in the Gürbe basin – provided that the sediment is sufficiently well mixed and that the corresponding cosmogenic nuclides are in an isotopic steady state (Clapuyt et al., 2019).
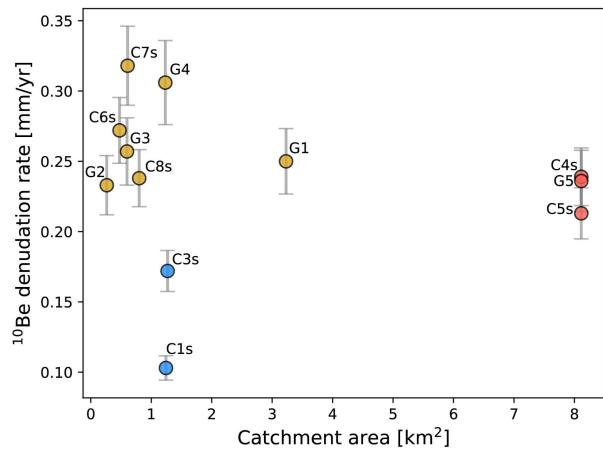
460 **Figure 6: Scale dependency of erosion rate estimates with concentrations of in-situ 10Be.** The variety of erosion rates determined for the scales of small local catchments (blue for the upper zone and yellow for the lower zone) is averaged out for the samples collected at the fan apex (red) where concentrations of in-situ [10]Be characterise the mixed erosional signal of the entire catchment and thus for a larger scale.

5.2 Steadiness of the denudation signals across time scales

Concentrations of cosmogenic nuclides in riverine quartz have the potential to record the erosional history of a landscape,
465 provided that (i) the nuclide production has occurred at a steady rate across the spatio-temporal scale over which they integrate erosion rates, and (ii) the nuclides are saturated (e.g., von Blanckenburg, 2005). A potential deviation from these assumptions could be caused by a sedimentary legacy from past glaciations (Jautzy et al., 2024). This also concerns the Gürbe basin, as the study area has a history of erosion and material deposition by local and regional glaciers – most notably by the Aare glacier. The coverage of the surface by glaciers could have led to transient shielding of the surface during glacial times, potentially
470 distorting the cosmogenic isotope signal (Slosson et al., 2022). Yet our [10]Be and [26]Al-based denudation rates point to an integration time < 8,000 years, whereas for ^{14}C, it is even shorter with < 3,000 years (Table S6). These ages are significantly younger than the last major glacial advance at around 12-11 ka ago (Ivy-Ochs et al., 2009). Therefore, we conclude that a potential inheritance from pre-glacial surfaces does not significantly affect our data for all nuclides.

A further potential bias in quantifying denudation rates with cosmogenic nuclides could be introduced through sediment
storage and reworking along the sediment cascade (e.g., Wittmann et al., 2020; Halsted et al., 2024). However, the ratios of
the ^{10}Be and ^{26}Al concentrations are close to the values characterizing a nuclide production close to the surface (Fig. 7).
Additionally, the resulting denudation rates are overall in good agreement with each other, at least in the upper zone and at the
basin's outlet. This suggests that the ^{10}Be and ^{26}Al concentrations do not record the occurrence of a significant erosional
transience during the past millennia, at least if the nuclide concentrations in the samples from the upper zone and the
downstream end of the Gürbe basin are considered. We therefore consider, and this has already been noted in the previous
section, that the signals preserved by the concentrations of in-situ ^{10}Be and ^{26}Al do record a pattern of erosion and sediment
generation that has been stable at least during the erosional timescale of both isotopes, which are several thousand years. We
acknowledge, that in the lower zone the supply of material through landsliding does result in a measurable discrepancy between
the ^{10}Be and ^{26}Al-based denudation rates (Figs. 4, 6 and 7), a pattern which is discussed in section 5.4. We also note that the
denudation rate pattern of the short-lived ^{14}C is distinctly different from that of ^{10}Be and ^{26}Al, which renders interpretations
thereof more complex (see next section 5.3).
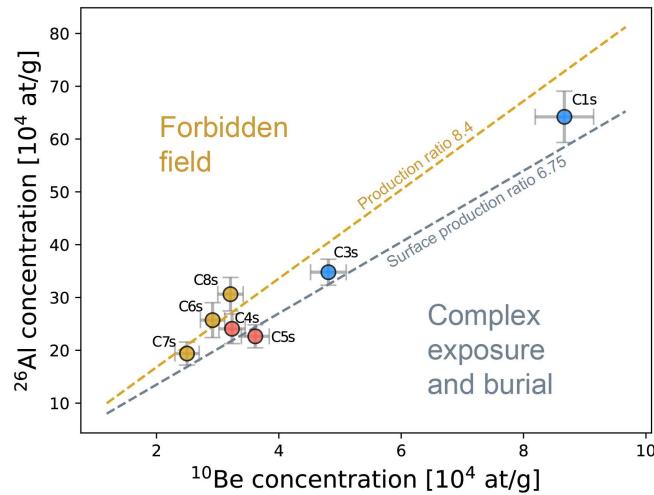
Figure 7: Two-nuclide diagram showing the ^{10}Be concentrations versus the ^{26}Al concentrations. The ^{26}Al concentration is plotted
against the ^{10}Be concentration. The concentrations are within the field that is characteristic for a nuclide production on the surface. The
occurrence of long-term burial can be excluded for our samples.

5.3 Potential controls on the pattern of cosmogenic ^{14}C

Here, we present several arguments as to why the pattern of ^{14}C concentrations in the riverine sediments of the Gürbe basin is
not straightforward to explain. First, as outlined by Hippe (2017), in cases where the signal integration timespan exceeds the
half-life of the corresponding cosmogenic isotope, a portion of the accumulated radionuclides will decay before the material
is completely eroded. The result is a reduction of the ^{14}C concentrations, which could lead to an artificially high erosion rate
(Hippe, 2017). In our case, the minimum exposure time required to accumulate the observed ^{14}C concentrations is less than

3,000 years – well below the isotope's half-life of 5,730 years. This makes unaccounted radioactive decay an unlikely primary cause of the low ^{14}C concentrations in our samples. Second, a recent change in erosion rates on timescales shorter than the signal integration-time of ^{10}Be and ^{26}Al could explain why the ^{14}C-based denudation rates are up to three times higher than the estimates derived from the other isotopes. This would require a scenario where the ^{14}C signal is already recording this increase in denudation, while the concentrations of ^{10}Be and ^{26}Al have not yet registered such a change. However, in rapidly eroding landscapes (> 500 mm/kyr) ^{10}Be concentrations initially adjust more rapidly to changes in erosion rates than ^{14}C concentrations (Skov et al., 2019). This difference arises from the higher muogenic production of ^{14}C at depth, which can cause a temporary increase of ^{14}C concentrations relative to ^{10}Be in freshly exposed bedrock and detrital material during periods of accelerated erosion. As a consequence, an acceleration of erosion can only be reliably detected several thousand years after the change (Skov et al., 2019; see also Mudd, 2017). The exact duration of this latency depends on both the magnitude and timing of the perturbation that caused the change. In other words, a scenario in which a period of accelerated erosion began several thousand years ago could explain why some ^{14}C-based denudation rates are higher than those derived from the other two nuclides. Yet, it does not explain the relative differences in ^{14}C-based denudation rates between the sampled catchments (Figs. 4 and 5). Particularly, the pattern is not consistent throughout any of the three zones, and the denudation rate variation within the zones is higher than the variation between the zones (Fig. 4). This would require a scenario in which the increase in erosion rates was different in magnitude and timing across all sub-catchments. Therefore, the inconsistent spatial pattern, along with greater within-zone than between-zone variations, suggests that the observed changes in ^{14}C concentrations cannot be explained solely by an increase in erosion rates. Third, geomorphic processes such as soil mixing or intermittent sediment storage during transport could in part explain the observed differences between the ^{14}C and ^{10}Be/^{26}Al-derived denudation rates. In particular, sediment could be stored – e.g., in response to landsliding – below the production zone of ^{14}C, during which the ^{14}C inventory is partially lost due to the radioactive decay of this isotope (Hippe et al., 2012; Kober et al., 2012; Hippe, 2017; Skov et al., 2019). Such a process has been referred to as transient shielding by Slosson et al. (2022). Because the ^{10}Be/^{14}C ratios in the Altiplano samples range between 3.6 and 15.2 – significantly higher than the surface production ratio of 0.31 – Hippe et al. (2012) interpreted the relatively low ^{14}C concentrations in the riverine sediments as a record of storage rather than surface erosion. However, since the ^{10}Be/^{14}C ratios of the riverine samples in the Gürbe basin range from 0.4 to 0.75 (Fig. 8) and thus do not fully fall within the complex exposure field, we consider it unlikely that the ^{14}C concentrations primarily reflect a signal of sedimentary storage. Furthermore, in the upper zone of the Gürbe basin, we exclude the occurrence of widespread storage following sediment mobilization, as there is no evidence in the landscape that such processes have taken place (e.g., the presence of large sedimentary bodies along the channels or talus cones as was reported by Slosson et al. (2022) from their study area). In summary, while ^{14}C has the potential to provide valuable insights into shifts in erosional dynamics, sediment storage, and episodic mobilization of material from deeper levels (Hippe et al., 2012; Hippe, 2017), we are unable to conclusively determine the specific processes responsible for the observed pattern of ^{14}C concentrations and denudation rates in the Gürbe basin.
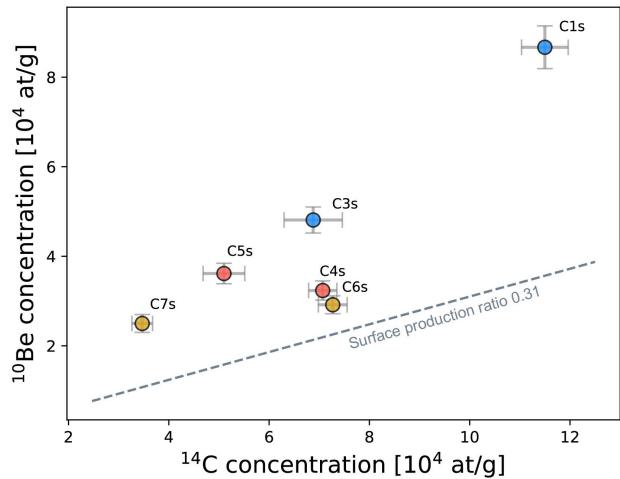
Figure 8: Two-nuclide diagram showing the [10]Be concentrations versus the ^{14}C concentrations. The [10]Be concentration is plotted against the ^{14}C concentration in relation to the surface production rate of 0.31 104 at/g (Hippe et al., 2012).

5.4 Landscape architecture and corresponding [10]Be and [26]Al signals

535 The comparison of the geomorphic map with the [10]Be and [26]Al concentrations and the calculated denudation rates exhibits a distinct difference between the upper and lower zone, each characterised by specific topographic features and dominant erosional processes. Specifically, the landscape in the upper zone of the Gürbe catchment is characterised by smooth slopes and the occurrence of partly incised channels with low steepness values and a low connectivity to the hillslopes. Such properties are characteristic for a landscape where overland flow erosion, also referred as hillslope diffusion according to Tucker and

540 Slingerland (1997), have controlled the generation of clastic sedimentary material (van den Berg et al., 2012). The high cosmogenic nuclide concentrations and, as consequence, the low denudation rates together with the [26]Al/[10]Be concentration ratios of 7.41 ± 0.69 and 7.23 ± 0.67 – that are close to the surface production ratio of 6.75 (Balco et al., 2008; Nishiizumi et al., 1989) – are consistent with such an interpretation (Figs. 7). The similarity in the denudation rates calculated for the two long-lived nuclides supports the interpretation of an erosional regime without significant perturbations (Fig. 9a), at least for

545 the time scale of thousands of years as recorded by both isotopes. We note that shallow landslides and localised rockfall do occur in this upper zone, but the resulting deposits are partly disconnected from the channel network, thereby minimizing their impact on the sediment budget of the Gürbe catchment (Fig. 2 & 3). In contrast, the lower zone exhibits a more dynamic erosional regime, where steeper slopes (20° to 25°) together with the predominant occurrence of mudstones in the Flysch and Upper Marine Molasse bedrock (Diem, 1986) offer ideal conditions for the displacement of medium- to deep-seated landslides.

550 Mapping also shows that landslides have impacted the sediment budget of the Gürbe River either through direct material supply into the main channel, where material is subsequently remobilised and transported downstream, or through erosion of landslide bodies by tributary streams and associated hillslope processes such as overland flow erosion and shallow-seated landslides, thereby reworking the previously displaced material. In general, such stochastic processes results in episodic

sediment inputs with relatively low [10]Be concentrations, as material is exhumed fast from greater depths (e.g., Niemi et al., 2005). In the Gürbe basin, however, most landslides have remained dormant for decades, but have regularly been re-activated with slip rates of several meters per day. These re-activations have resulted in the excavation of material along multiple trajectories from depth to the surface, and finally to the channel network. The mixing of material from different exposure trajectories (Fig. 9b) most likely explains the relatively high [26]Al/[10]Be concentration ratios between 7.76 ± 1.07 to 9.54 ± 1.17 (Fig. 6) that we determined for the riverine material in three tributaries with material sources in these landslides. The discrepancy between the [10]Be- and [26]Al-based erosion rates – with ratios ranging from 1.1 to 1.4 – is a further support of the inferred complex erosional history along the sediment cascade (Fig. 9a). These findings demonstrate that the occurrence of landsliding not only results in an overall increase of erosion rates but also introduces a variability in the cosmogenic [26]Al/[10]Be concentration ratios. Yet, if such cycles of landslide quiescence and activity have occurred multiple times and at different locations in a basin, the resulting cosmogenic concentrations will converge to a stable cosmogenic signal farther downstream and thus for a large spatial scale. This is the case for the outlet of the Gürbe basin where we determine consistent cosmogenic nuclide signals. This implies that at the scale of individual tributary basins, which is < 2 km^2 in our case, the production of sediment can be highly stochastic. At the scale of an entire basin – in our case the Gürbe basin with a size of 8 km^2 – the ensemble of the stochastic processes converges to a sediment cascade that can be characterized as steady state, at least for the time scale recorded by the cosmogenic isotopes.
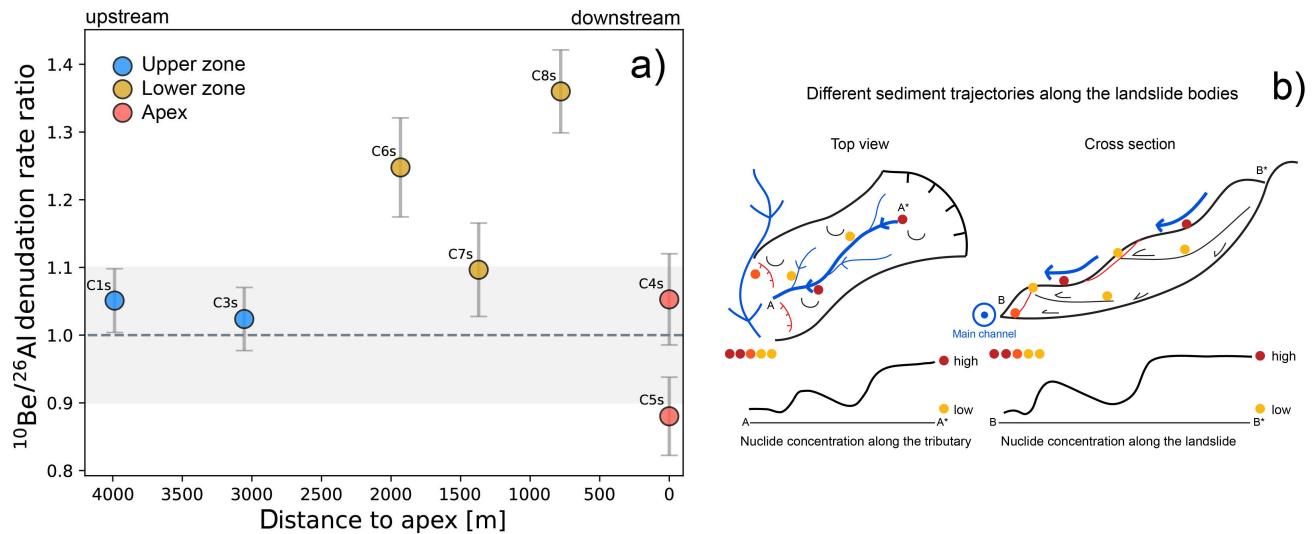
Figure 9: Sediment cascade in the Gürbe basin recorded by cosmogenic nuclides (a) Ratios between [26]Al- and [10]Be-based denudation rates. In the upper zone the ratios between the denudation rate calculated with both isotopes are in very good agreement. In the lower zone the [26]Al-based denudation rates are lower than the [10]Be-based rate, leading to ratios that are larger than one. At the fan apex the ratios between both rates are in a relatively good agreement. The grey shading is representing the ± 10% envelope of the isotope ratio. (b) conceptual model of different sediment trajectories along the medium- to deep-seated landslide bodies leading to lower nuclide concentrations in tributaries.

5.5 The importance of glacial conditioning as an erosional driving force

In a previous study, Delunel et al. (2020) showed that a large part of the catchment-averaged denudation rates in the European Alps can be understood as a diffusion-type of process – or a mechanism which we refer to as overland flow erosion following Battista et al. (2020) – where denudation rates increase with mean-basin hillslope angles until a threshold hillslope angle of 25°-30° (Schlunegger and Norton, 2013). Because the hillslope angles in the Gürbe catchment are below the 25° threshold, one would predict an erosional signal that could be explained by such a mechanism. While all our denudation rates do fall in the corresponding range of denudation rates (cf. Fig. 5 of Delunel et al., 2020) and since such an assignment is certainly correct for the upper part of the Gürbe catchment (section 5.4), the lower zone deviates from this acknowledgably useful categorization. Indeed, despite the slopes being flatter than 25°, erosion in this region has been dominated by deep-seated landslides that are perched by a channel network. Such a combination of processes has typically been reported for landscapes steeper than 30° in the European Alps (Delunel et al., 2020) and other mountain ranges, e.g. the San Gabriel Mountains (DiBiase et al., 2023). This difference of erosion highlights the importance of another driving force than lithology alone because Flysch bedrock also occurs in the upper zone where landslides are largely absent, but where the hillslopes are less steep. Because the elevation of the knickzone separating the upper from the lower zones corresponds to the level of the LGM Aare glacier in this region (Bini et al., 2009), it is possible that the formation of the knickzone along the Gürbe River was conditioned by glacial carving during the LGM and possibly previous glaciations. Accordingly, the relatively flat channel and hillslope morphology in the area upstream of the knickzone could be explained by damming effects related to the presence of the Aare glacier. In contrast, the shape of the topography downstream of the knickzone was most likely conditioned by erosion along the lateral margin of the Aare glacier. Accordingly, the formation of a relatively steep flank could explain why the course of the Gürbe River is steeper than would be expected for a river with a same catchment size (do Prado et al., 2024), and why erosion on the hillslopes has been dominated by landsliding instead of overland flow erosion. Similar controls were already proposed by Norton et al. (2010) and van den Berg et al. (2012) upon explaining the occurrence of landscapes dominated by gentle hillslopes upstream of glacially conditioned knickzones and steeper hillslopes downstream of them. In such a context, a lowering of the base level after the retreat of the LGM glacier would have initiated a wave of headward erosion, with the consequence that the entire catchment is in a transient stage of landscape evolution (Abbühl et al., 2011; Vanacker et al., 2015). Accordingly, while the Gurnigel Flysch and Lower Marine Molasse bedrock seem to promote the occurrence deep-seated landslides – thus overriding the expected overland flow-controlled behaviour typically observed in catchments with similar slopes elsewhere – a steeping of the landscape due to glacial carving needs also be considered as an additional condition accelerating erosion in the lower part of the basin.

5.6 Geochemical composition of the detrital material, and the use of cosmogenic isotopes for provenance tracing

The whole rock geochemical analysis discloses a picture that is characteristic for a basin where limestones and sandstones are the main lithological constituents, as already demonstrated by Glaus et al. (2019) and Da Silva Guimarães et al. (2021) for other basins in the Alps. Yet, in contrast to the aforementioned studies, the results of our research did not allow a differentiation of the erosional signals derived from the various parts of the Gürbe basin, because here the only difference in composition among the samples seems to relate to the relative proportion of limestone constituents in the detrital material (section 4.4). However, the outcropping limestone units are only present locally in some of the headwater reaches (Fig. 2). This introduces a potential limitation: while our quartz-based cosmogenic nuclide measurements provide valuable erosion rate estimates, they are inherently blind to sediment generated from quartz-free lithologies, such as limestones. This raises the question of how well the total sediment load and the erosion rates – the latter ones inferred from the cosmogenic nuclide data – are in agreement with each other. In particular, high erosion rates in the headwater areas made up of limestones could lead to a high relative abundance of limestone grains in the Gürbe sediments farther downstream. This, in turn, could result in an underestimation of the effective denudation rates if such budgets are only based on cosmogenic isotopes. However, in our case, we observe only a limited contribution of the limestone lithologies to the sediment budget of the entire Gürbe basin as we do not see any systematic variation in the geochemical composition of the detrital material. We therefore consider our cosmogenic-based erosion rates as representative – particularly as we use them to map spatial variations in the generation of sediment across the basin. Additonally, and more important, the use of paired nuclides – in our case ^{26}Al to ^{10}Be – yields conclusive information on the origin of the detrital material as sediments derived from landslides and thus from deeper levels tend to have a higher ratio between the concentrations of both isotopes than sedimentary particles generated through overland flow erosion alone (Akçar et al., 2017; Dingle et al., 2018; Knudsen et al., 2020). Accordingly, this study demonstrates that concentrations of cosmogenic isotopes offer suitable information for allocating the source of sediments in drainage basins where other provenance tracing methods, in our case whole-rock geochemical compositions of the riverine material, yield non-conclusive results. Here, we demonstrate that such approach to trace the origin of the material holds even in a basin where the spatial contrasts in measured erosion rates are relatively low. In such cases, a reconstruction of both the sediment sources and the associated erosional mechanisms requires a dense sampling strategy, as implemented in this work – a need that was already emphasised by Clapuyt et al. (2019) and Battista et al. (2020).

Conclusions

635   This study demonstrates that cosmogenic nuclides are ideal tracers for identifying the origin of detrital material in basins with spatially varying erosion rates. They not only allow us to determine the region where most sediment has been generated, but also yield crucial information to reconstruct the mechanisms through which erosion has occurred (e.g., overland flow erosion versus landsliding), particularly when multiple isotopes are used. In the Gürbe basin, we were able to reconstruct such patterns and mechanisms using concentrations of in-situ ^{10}Be and ^{26}Al measured in riverine quartz. However, the concentrations of in-

640 situ ^{14}C, which we also measured in the same samples, yielded non-conclusive results. Also in the Gürbe basin, we found that the erosional processes were different in the upper zone above the LGM trim line where the landscape is flat and sediment generation has been dominated by overland flow erosion, and in the region below it where the landscape is steeper and erosion has been accomplished by landsliding and fluvial incision. This points to a legacy of the current erosional mechanisms stemming from the glaciations, where carving of the valley flanks by the LGM (Late Glacial Maximum) and earlier glaciers

645 steepened the landscape, thereby promoting erosion below the LGM margin following the glaciers' retreat. This initiated a wave of headward retreat and the formation of an erosional front separating an upper part with low erosion rates (overland flow erosion) from a lower part where erosion occurs more rapidly and has mainly been accomplished by landsliding. In the Gürbe basin, we identified this erosional front through the occurrence of a distinct knickzone in the longitudinal stream profile. This phase of headward retreat thus suggests that the Gürbe basin has been in a long-term transient state of topographic

650 development where the current accelerated erosion and landsliding in the lower zone has been glacially conditioned. Yet despite this transient state of basin development, we find – based on the concentrations of cosmogenic ^{10}Be and ^{26}Al in the riverine material – that the pattern and rate of sediment generation has been quite stable and thus steady during the past thousands of years. This was surprising because landslides have the potential to introduce a stochasticity in the way of how erosion and sediment generation occurs. It thus appears that the transient adjustment of the Gürbe basin to post-glacial

655 conditions has occurred in a near-steady, possibly self-organised way, resulting in sediment generation, which has occurred at nearly constant rates at least during the past thousands of years. Because cosmogenic ^{26}Al and ^{10}Be integrate erosional signals over millennia in the Gürbe basin—including periods during which environmental conditions have changed—we expect a similar pattern of sediment generation and transfer in the near future, even under the current warming climate. Consequently, in the near future, the local authorities are likely to face the same sediment transfer mechanisms through the basin and the

660 cascade of check dams as those occurring today.

Author contributions

CS designed the study, conducted the analyses and wrote the paper with support by FS, DM and BM. NA offered scientific advise during sample collection and preparation, and during the analysis of the AMS results. MC, CV, PG supervised the AMS measurements of 26Al and 10Be and offered support for the interpretation of the MS data. NH performed the in-situ ^{14}C extraction and measured the 14C concentrations. All authors contributed to the scientific processing and discussion of the results and to the drafting of the paper.

Competing interests

The authors declare that they have no conflict of interest

Data availability

All data used in this study are provided in tables or included in the Supplementary Materials. The swisstopo digital elevation models (DEMs) are publicly available.

Acknowledgements

We thank Julijana Gajic for training and supervising the lab work at the IFG as well as Priska Bähler for the total Al measurements. This work was funded through the Trebridge project funded by the Swiss National Science Foundation (SNSF project No 205912).

References

680 Abbühl, L. M., Norton, K. P., Jansen, J. D., Schlunegger, F., Aldahan, A., and Possnert, G.: Erosion rates and mechanisms of knickzone retreat inferred from 10 Be measured across strong climate gradients on the northern and central Andes Western Escarpment, Earth Surf. Process. Landforms, 36, 1464–1473, https://doi.org/10.1002/esp.2164, 2011.

Akçar, N., Ivy-Ochs, S., Alfimov, V., Schlunegger, F., Claude, A., Reber, R., Christl, M., Vockenhuber, C., Dehnert, A., Rahn, M., and Schlüchter, C.: Isochron-burial dating of glaciofluvial deposits: First results from the Swiss Alps, Earth

685 Surf. Process. Landforms, 42, 2414–2425, https://doi.org/10.1002/esp.4201, 2017.

Balco, G., Stone, J. O., Lifton, N. A., and Dunai, T. J.: A complete and easily accessible means of calculating surface exposure ages or erosion rates from 10Be and 26Al measurements, Quaternary Geochronology, 3, 174–195, https://doi.org/10.1016/j.quageo.2007.12.001, 2008.

Battista, G., Schlunegger, F., Burlando, P., and Molnar, P.: Modelling localized sources of sediment in mountain catchments

690 for provenance studies, Earth Surf. Process. Landforms, 45, 3475–3487, https://doi.org/10.1002/esp.4979, 2020.

Bierman, P. and Steig, E.: Estimating rates of denudation using cosmogenic isotope abundances in sediment, Earth Surf. Process. Landforms, 21, 125–139, 1996.

Bini, A., Buonchristiani, J.-F., Couterand, S., Ellwanger, D., Felber, M., Florineth, D., Graf, H. R., Keller, O., Kelly, M., Schlüchter, C., and and Schöneich, P.: Die Schweiz während des letzteiszeitlichen Maximums (LGM),

695 https://www.swisstopo.admin.ch/de (last access: 6 December 2024), 2009.

Binnie, S., Pjillips, W., Summerfield, M., and Fifield, Keith Fifield, L.: Sediment mixing and basin-wide cosmogenic nuclide analysis in rapidly eroding mountainous environments, Quaternary Geochronology, 1, 4–14, https://doi.org/10.1016/j.quageo.2006.06.013, 2006.

Borselli, L., Cassi, P., and Torri, D.: Prolegomena to sediment and flow connectivity in the landscape: A GIS and field

700 numerical assessment, CATENA, 75, 268–277, https://doi.org/10.1016/j.catena.2008.07.006, 2008.

Brardinoni, F., Grischott, R., Kober, F., Morelli, C., and Christl, M.: Evaluating debris-flow and anthropogenic disturbance on 10 Be concentration in mountain drainage basins: implications for functional connectivity and denudation rates across time scales, Earth Surf. Process. Landforms, 45, 3955–3974, https://doi.org/10.1002/esp.5012, 2020.

Bundesamt für Landestopografie swisstopo, Tarquini S., I. Isola, M. Favalli, A. Battistini, and G. Dotta: TINITALY, a

705 digital elevation model of Italy with a 10 meters cell size (Version 1.1). Istituto Nazionale di Geofisica e Vulcanologia (INGV). https://doi.org/10.13127/tinitaly/1.1; DGM Österreich, geoland.at; DGM1, Bayerische Vermessungsverwaltung – www.geodaten.bayern.de; EU-DEM, provided under COPERNICUS by the European Union and ESA, all rights reserved; RGEAlti, Institut National de l'information géographique et forestière, données originales tétéchargées sur https://geoservices.ign.fr/rgealti#telechargement5m, mise à jour du juillet 2023, 2023.

710 Cavalli, M., Trevisani, S., Comiti, F., and Marchi, L.: Geomorphometric assessment of spatial sediment connectivity in small Alpine catchments, Geomorphology, 188, 31–41, https://doi.org/10.1016/j.geomorph.2012.05.007, 2013.

Chittenden, H., Delunel, R., Schlunegger, F., Akçar, N., and Kubik, P.: The influence of bedrock orientation on the landscape evolution, surface morphology and denudation (10 Be) at the Niesen, Switzerland, Earth Surf. Process. Landforms, 39, 1153–1166, https://doi.org/10.1002/esp.3511, 2014.

715 Clapuyt, F., Vanacker, V., Christl, M., van Oost, K., and Schlunegger, F.: Spatio-temporal dynamics of sediment transfer systems in landslide-prone Alpine catchments, Solid Earth, 10, 1489–1503, https://doi.org/10.5194/se-10-1489-2019, 2019.

Cruz Nunes, F., Delunel, R., Schlunegger, F., Akçar, N., and Kubik, P. W.: Bedrock bedding, landsliding and erosional budgets in the Central European Alps, Terra Nova, 27, 370–378, https://doi.org/10.1111/ter.12169, 2015.

720 Da Silva Guimarães, E., Delunel, R., Schlunegger, F., Akçar, N., Stutenbecker, L., and Christl, M.: Cosmogenic and Geological Evidence for the Occurrence of a Ma-Long Feedback between Uplift and Denudation, Chur Region, Swiss Alps, Geosciences, 11, 339, https://doi.org/10.3390/geosciences11080339, 2021.

Delunel, R., Schlunegger, F., Valla, P. G., Dixon, J., Glotzbach, C., Hippe, K., Kober, F., Molliex, S., Norton, K. P., Salcher, B., Wittmann, H., Akçar, N., and Christl, M.: Late-Pleistocene catchment-wide denudation patterns across the European 725 Alps, Earth-Science Reviews, 211, 103407, https://doi.org/10.1016/j.earscirev.2020.103407, 2020.

Delunel, R., Bourlès, D. L., van der Beek, P. A., Schlunegger, F., Leya, I., Masarik, J., and Paquet, E.: Snow shielding factors for cosmogenic nuclide dating inferred from long-term neutron detector monitoring, Quaternary Geochronology, 24, 16–26, https://doi.org/10.1016/j.quageo.2014.07.003, 2014.

Delunel, R., van der Beek, P. A., Carcaillet, J., Bourlès, D. L., and Valla, P. G.: Frost-cracking control on catchment 730 denudation rates: Insights from in situ produced 10Be concentrations in stream sediments (Ecrins–Pelvoux massif, French Western Alps), Earth and Planetary Science Letters, 293, 72–83, https://doi.org/10.1016/j.epsl.2010.02.020, 2010.

DiBiase, R. A.: Short communication: Increasing vertical attenuation length of cosmogenic nuclide production on steep slopes negates topographic shielding corrections for catchment erosion rates, Earth Surf. Dynam., 6, 923–931, 735 https://doi.org/10.5194/esurf-6-923-2018, 2018.

DiBiase, R. A., Neely, A. B., Whipple, K. X., Heimsath, A. M., and Niemi, N. A.: Hillslope Morphology Drives Variability of Detrital 10 Be Erosion Rates in Steep Landscapes, Geophysical Research Letters, 50, https://doi.org/10.1029/2023GL104392, 2023.

DiBiase, R. A., Whipple, K. X., Heimsath, A. M., and Ouimet, W. B.: Landscape form and millennial erosion rates in the 740 San Gabriel Mountains, CA, Earth and Planetary Science Letters, 289, 134–144, https://doi.org/10.1016/j.epsl.2009.10.036, 2010.

Diem, B.: Die Untere Meeresmolasse zwischen der Saane (Westschweiz) und der Ammer (Oberbayern)., Exlogae Geol. Helv., 493–559, 1986.

Dingle, E. H., Sinclair, H. D., Attal, M., Rodés, Á., and Singh, V.: Temporal variability in detrital [10]Be concentrations in a large Himalayan catchment, Earth Surf. Dynam., 6, 611–635, https://doi.org/10.5194/esurf-6-611-2018, 2018.

do Prado, A. H., Mair, D., Garefalakis, P., Schmidt, C., Whittaker, A., Castelltort, S., and Schlunegger, F.: Check dam impact on sediment loads: example of the Guerbe River in the Swiss Alps – a catchment scale experiment, Hydrol. Earth Syst. Sci., 28, 1173–1190, https://doi.org/10.5194/hess-28-1173-2024, 2024.

Frei, P., Kotlarski, S., Liniger, M. A., and Schär, C.: Future snowfall in the Alps: projections based on the EURO-CORDEX regional climate models, The Cryosphere, 12, 1–24, https://doi.org/10.5194/tc-12-1-2018, 2018.

Glaus, G., Delunel, R., Stutenbecker, L., Akçar, N., Christl, M., and Schlunegger, F.: Differential erosion and sediment fluxes in the Landquart basin and possible relationships to lithology and tectonic controls, Swiss J Geosci, 112, 453–473, https://doi.org/10.1007/s00015-019-00344-3, 2019.

Granger, D. E., Kirchner, J. W., and Finkel, R.: Spatially Averaged Long-Term Erosion Rates Measured from in Situ-Produced Cosmogenic Nuclides in Alluvial Sediment, The Journal of Geology, 104, 249–257, https://doi.org/10.1086/629823, 1996.

Haldimann, P., Graf, H. R., Jost, J., and Kälin, D. (Eds.): 1071 Bülach, Geologischer Atlas der Schweiz, 151 = Blatt 1071, Bundesamt für Landestopografie swisstopo Geologische Landesaufnahme, Wabern, 2017.

Halsted, C., Bierman, P., Codilean, A., Corbett, L., and Caffee, M.: Global analysis of in situ cosmogenic 26 Al/ 10 Be ratios in fluvial sediments indicates widespread sediment storage and burial during transport, https://doi.org/10.5194/gchron-2024-22, 2024.

Heinz, R. A., Blau, R. V., Nicol, G., and Burkhalter, R.: Thun, Geologischer Atlas der Schweiz 1, 177 = Blatt 1207, Bundesamt für Landestopografie swisstopo, Wabern, 2023.

Hippe, K., Kober, F., Wacker, L., Fahrni, S. M., Ivy-Ochs, S., Akçar, N., Schlüchter, C., and Wieler, R.: An update on in situ cosmogenic 14C analysis at ETH Zürich, Nuclear Instruments and Methods in Physics Research Section B: Beam Interactions with Materials and Atoms, 294, 81–86, https://doi.org/10.1016/j.nimb.2012.06.020, 2013.

Hippe, K.: Constraining processes of landscape change with combined in situ cosmogenic 14C-10Be analysis, Quaternary Science Reviews, 173, 1–19, https://doi.org/10.1016/j.quascirev.2017.07.020, 2017.

Hippe, K. and Lifton, N. A.: Calculating Isotope Ratios and Nuclide Concentrations for In Situ Cosmogenic 14 C Analyses, Radiocarbon, 56, 1167–1174, https://doi.org/10.2458/56.17917, 2014.

Hippe, K., Gordijn, T., Picotti, V., Hajdas, I., Jansen, J. D., Christl, M., Vockenhuber, C., Maden, C., Akçar, N., and Ivy-Ochs, S.: Fluvial dynamics and 14 C- 10 Be disequilibrium on the Bolivian Altiplano, Earth Surf. Process. Landforms, 44, 766–780, https://doi.org/10.1002/esp.4529, 2019.

Hippe, K., Kober, F., Zeilinger, G., Ivy-Ochs, S., Maden, C., Wacker, L., Kubik, P. W., and Wieler, R.: Quantifying denudation rates and sediment storage on the eastern Altiplano, Bolivia, using cosmogenic 10Be, 26Al, and in situ 14C, Geomorphology, 179, 58–70, https://doi.org/10.1016/j.geomorph.2012.07.031, 2012.

Ivy-Ochs, S., Monegato, G., and Reitner, J. M.: The Alps: glacial landforms from the Last Glacial Maximum, 449–460, https://doi.org/10.1016/B978-0-12-823498-3.00030-3, 2022.

Ivy-Ochs, S., Kerschner, H., Maisch, M., Christl, M., Kubik, P. W., and Schlüchter, C.: Latest Pleistocene and Holocene
780   glacier variations in the European Alps, Quaternary Science Reviews, 28, 2137–2149, https://doi.org/10.1016/j.quascirev.2009.03.009, 2009.

Jäckle, S.: Hydrologischer atlas der Schweiz. Wildbach Gürbe Gurnigel – Wattenwil, Vol. 6.1, Bern, Switzerland, Bern, available at: https://hydrologischeratlas. ch/produkte/exkursionen/bern/61, last access: March 2024, 2013.

Jautzy, T., Rixhon, G., Braucher, R., Delunel, R., Valla, P. G., Schmitt, L., and Team, A.: Cosmogenic (un-)steadiness
785   revealed by paired-nuclide catchment-wide denudation rates in the formerly half-glaciated Vosges Mountains (NE France), Earth and Planetary Science Letters, 625, 118490, https://doi.org/10.1016/j.epsl.2023.118490, 2024.

Jonas, T., Marty, C., and Magnusson, J.: Estimating the snow water equivalent from snow depth measurements in the Swiss Alps, Journal of Hydrology, 378, 161–167, https://doi.org/10.1016/j.jhydrol.2009.09.021, 2009.

Knudsen, M. F., Nørgaard, J., Grischott, R., Kober, F., Egholm, D. L., Hansen, T. M., and Jansen, J. D.: New cosmogenic
790   nuclide burial-dating model indicates onset of major glaciations in the Alps during Middle Pleistocene Transition, Earth and Planetary Science Letters, 549, 116491, https://doi.org/10.1016/j.epsl.2020.116491, 2020.

Kober, F., Hippe, K., Salcher, B., Ivy-Ochs, S., Kubik, P. W., Wacker, L., and Hählen, N.: Debris-flow-dependent variation of cosmogenically derived catchment-wide denudation rates, Geology, 2012, 935–938, 2012.

Kubik, P. W. and Christl, M.: 10Be and 26Al measurements at the Zurich 6MV Tandem AMS facility, Nuclear Instruments
795   and Methods in Physics Research Section B: Beam Interactions with Materials and Atoms, 268, 880–883, https://doi.org/10.1016/j.nimb.2009.10.054, 2010.

Lal, D.: Cosmic ray labeling of erosion surfaces: in situ nuclide production rates and erosion models, Earth and Planetary Science Letters, 104, 424–439, https://doi.org/10.1016/0012-821X(91)90220-C, 1991.

Latif, I.: Denudation Rates, Sediment Supply and Grain Size Pattern in an Anthropogenically Influenced Torrent, Central
800   Alps, Switzerland., Upublished Ms thesis, Institute of Geological Sciences, University of Bern, Bern, 2019.

Lupker, M., Hippe, K., Wacker, L., Steinemann, O., Tikhomirov, D., Maden, C., Haghipour, N., and Synal, H.-A.: In-situ cosmogenic 14C analysis at ETH Zürich: Characterization and performance of a new extraction system, Nuclear Instruments and Methods in Physics Research Section B: Beam Interactions with Materials and Atoms, 457, 30–36, https://doi.org/10.1016/j.nimb.2019.07.028, 2019.

805 Marc, O., Behling, R., Andermann, C., Turowski, J. M., Illien, L., Roessner, S., and Hovius, N.: Long-term erosion of the Nepal Himalayas by bedrock landsliding: the role of monsoons, earthquakes and giant landslides, Earth Surf. Dynam., 7, 107–128, https://doi.org/10.5194/esurf-7-107-2019, 2019.

Maxeiner, S., Synal, H.-A., Christl, M., Suter, M., Müller, A., and Vockenhuber, C.: Proof-of-principle of a compact 300 kV multi-isotope AMS facility, Nuclear Instruments and Methods in Physics Research Section B: Beam Interactions with
810   Materials and Atoms, 439, 84–89, https://doi.org/10.1016/j.nimb.2018.11.028, 2019.

Mudd, S. M.: Detection of transience in eroding landscapes, Earth Surf. Process. Landforms, 42, 24–41, https://doi.org/10.1002/esp.3923, 2017.

NGKAT: Naturgefahrenkataster, Amt für Wald und Naturgefahren des Kantons Bern, https://www.agi.dij.be.ch/de/start/geoportal/geodaten/detail.html?type=geoproduct&code=NGKAT, last access: 2024, 2024.

Niemi, N. A., Oskin, M., Burbank, D. W., Heimsath, A. M., and Gabet, E. J.: Effects of bedrock landslides on cosmogenically determined erosion rates, Earth and Planetary Science Letters, 237, 480–498, https://doi.org/10.1016/j.epsl.2005.07.009, 2005.

Nishiizumi, K., Winterer, E. L., Kohl, C. P., Klein, J., Middleton, R., Lal, D., and Arnold, J. R.: Cosmic ray production rates of 10 Be and 26 Al in quartz from glacially polished rocks, J. Geophys. Res., 94, 17907–17915, https://doi.org/10.1029/JB094iB12p17907, 1989.

Norton, K. P., Abbühl, L. M., and Schlunegger, F.: Glacial conditioning as an erosional driving force in the Central Alps, Geology, 38, 655–658, https://doi.org/10.1130/G31102.1, 2010.

Pedregosa, F., Varoquaux, G., Gramfort, A., Michel, V., Thirion, B., Grisel, O., Blondel, M., Prettenhofer, P., Weiss, R., Dubourg, V., Vanderblas, J., Passos, A., and Cournapeau, D.: Scikit-learn: Machine Learning in Python, Journal of Machine Learning Research, 2825–2830, 2011.

Ramirez, J. A., Mertin, M., Peleg, N., Horton, P., Skinner, C., Zimmermann, M., and Keiler, M.: Modelling the long-term geomorphic response to check dam failures in an alpine channel with CAESAR-Lisflood, International Journal of Sediment Research, 37, 687–700, https://doi.org/10.1016/j.ijsrc.2022.04.005, 2022.

Reber, R., Delunel, R., Schlunegger, F., Litty, C., Madella, A., Akçar, N., and Christl, M.: Environmental controls on 10 Be-based catchment-averaged denudation rates along the western margin of the Peruvian Andes, Terra Nova, 29, 282–293, https://doi.org/10.1111/ter.12274, 2017.

Riley, S. J., DeGloria, S., and Elliot, R.: A Terrain Ruggedness Index that Quantifies Topographic Heterogeneity, Intermountain Journal of Sciences, 23–27, 1999.

Roda-Boluda, D. C., D'Arcy, M., Whittaker, A. C., Gheorghiu, D. M., and Rodés, Á.: 10Be erosion rates controlled by transient response to normal faulting through incision and landsliding, Earth and Planetary Science Letters, 507, 140–153, https://doi.org/10.1016/j.epsl.2018.11.032, 2019.

Salvisberg, M.: Taming the torrent: changes in flood protection at the Gürbe River (Switzerland) from the nineteenth century until today, Water history, 14, 355–377, https://doi.org/10.1007/s12685-022-00312-z, 2022.

Salvisberg, M.: Der Hochwasserschutz an der Gürbe: Eine Herausforderung für Generationen (1855-2010), Wirtschafts-, Sozial- und Umweltgeschichte (WSU), Band 7, Schwabe Verlag, Basel, 406 pp., 2017.

Savi, S., Delunel, R., and Schlunegger, F.: Efficiency of frost-cracking processes through space and time: An example from the eastern Italian Alps, Geomorphology, 232, 248–260, https://doi.org/10.1016/j.geomorph.2015.01.009, 2015.

Savi, S., Norton, K., Picotti, V., Brardinoni, F., Akçar, N., Kubik, P. W., Delunel, R., and Schlunegger, F.: Effects of sediment mixing on 10Be concentrations in the Zielbach catchment, central-eastern Italian Alps, Quaternary Geochronology, 19, 148–162, https://doi.org/10.1016/j.quageo.2013.01.006, 2014.

Schlunegger, F. and Garefalakis, P.: Einführung in die Sedimentologie, Schweitzerbart, Stuttgart, 305 pp., 2023.

Schlunegger, F. and Norton, K. P.: Water versus ice: The competing roles of modern climate and Pleistocene glacial erosion in the Central Alps of Switzerland, Tectonophysics, 602, 370–381, https://doi.org/10.1016/j.tecto.2013.03.027, 2013.

Schwanghart, W. and Scherler, D.: Short Communication: TopoToolbox 2 – MATLAB-based software for topographic analysis and modeling in Earth surface sciences, Earth Surf. Dynam., 2, 1–7, https://doi.org/10.5194/esurf-2-1-2014, 2014.

Sibson, R.: A Brief Description of Natural Neighbor Interpolation, in: Interpolating Multivariate Data, John Wiley & Sons, New York, 21–36, 1981.

Simpson, G. and Schlunegger, F.: Topographic evolution and morphology of surfaces evolving in response to coupled fluvial and hillslope sediment transport, J. Geophys. Res., 108, https://doi.org/10.1029/2002JB002162, 2003.

Skov, D. S., Egholm, D. L., Jansen, J. D., Sandiford, M., and Knudsen, M. F.: Detecting landscape transience with in situ cosmogenic 14C and 10Be, Quaternary Geochronology, 54, 101008, https://doi.org/10.1016/j.quageo.2019.101008, 2019.

Slosson, J. R., Hoke, G. D., and Lifton, N.: Non-Steady-State 14 C- 10 Be and Transient Hillslope Dynamics in Steep High Mountain Catchments, Geophysical Research Letters, 49, https://doi.org/10.1029/2022GL100365, 2022.

Starke, J., Ehlers, T. A., and Schaller, M.: Latitudinal effect of vegetation on erosion rates identified along western South America, Science (New York, N.Y.), 367, 1358–1361, https://doi.org/10.1126/science.aaz0840, 2020.

Stone, J. O.: Air pressure and cosmogenic isotope production, J. Geophys. Res., 105, 23753–23759, https://doi.org/10.1029/2000JB900181, 2000.

Stutenbecker, L., Delunel, R., Schlunegger, F., Silva, T. A., Šegvić, B., Girardclos, S., Bakker, M., Costa, A., Lane, S. N., Loizeau, J.-L., Molnar, P., Akçar, N., and Christl, M.: Reduced sediment supply in a fast eroding landscape? A multi-proxy sediment budget of the upper Rhône basin, Central Alps, Sedimentary Geology, 375, 105–119, https://doi.org/10.1016/j.sedgeo.2017.12.013, 2018.

Swisstopo: GeoCover, Federal Office of Topography swisstopo, https://www.swisstopo.admin.ch/en/geological-model-2d-geocover#GeoCover---Download, last access: 2024, 2024a.

Swisstopo: GeoMaps 500 Pixel, Federal Office of Topography swisstopo, https://www.swisstopo.admin.ch/en/geomaps-500-pixel, last access: 2024, 2024b.

Swisstopo: Swiss Map Raster 10, Federal Office of Topography swisstopo, https://www.swisstopo.admin.ch/de/landeskarte-swiss-map-raster-10, last access: 2024, 2024c.

Swisstopo: swissALTI3D, Federal Office of Topography swisstopo, https://www.swisstopo.admin.ch/en/height-model-swissalti3d, last access: 2024, 2024d.

Swisstopo: SWISSIMAGE 10 cm, Federal Office of Topography swisstopo, https://www.swisstopo.admin.ch/de/orthobilder-swissimage-10-cm, last access: 2024, 2024e.

880 Swisstopo: SWISSIMAGE HIST, Federal Office of Topography swisstopo, https://www.swisstopo.admin.ch/en/orthoimage-swissimage-hist, last access: 2024, 2024f.

Synal, H.-A., Stocker, M., and Suter, M.: MICADAS: A new compact radiocarbon AMS system, Nuclear Instruments and Methods in Physics Research Section B: Beam Interactions with Materials and Atoms, 259, 7–13, https://doi.org/10.1016/j.nimb.2007.01.138, 2007.

885 Tercier, P. J. and Bieri, P.: Gurnigel (AS 348 - 351, Guggisberg - Rüschegg - Plasselb - Gantrisch)., Sans notive explicative (Feuille entoilée, pliée), 1961.

Tucker, G. E. and Slingerland, R.: Drainage basin responses to climate change, Water Resour. Res., 33, 2031–2047, https://doi.org/10.1029/97WR00409, 1997.

van den Berg, F., Schlunegger, F., Akçar, N., and Kubik, P.: 10 Be-derived assessment of accelerated erosion in a glacially
890 conditioned inner gorge, Entlebuch, Central Alps of Switzerland, Earth Surf. Process. Landforms, 37, 1176–1188, https://doi.org/10.1002/esp.3237, 2012.

Vanacker, V., Blanckenburg, F. von, Govers, G., Molina, A., Campforts, B., and Kubik, P. W.: Transient river response, captured by channel steepness and its concavity, Geomorphology, 228, 234–243, https://doi.org/10.1016/j.geomorph.2014.09.013, 2015.

895 vonBlanckenburg, F.: The control mechanisms of erosion and weathering at basin scale from cosmogenic nuclides in river sediment, Earth and Planetary Science Letters, 237, 462–479, https://doi.org/10.1016/j.epsl.2005.06.030, 2005.

West, A. J., Hetzel, R., Li, G., Jin, Z., Zhang, F., Hilton, R. G., and Densmore, A. L.: Dilution of 10Be in detrital quartz by earthquake-induced landslides: Implications for determining denudation rates and potential to provide insights into landslide sediment dynamics, Earth and Planetary Science Letters, 396, 143–153,
900 https://doi.org/10.1016/j.epsl.2014.03.058, 2014.

Winkler, W.: Palaeocurrents and petrography of the Gurnigel-Schlieren flysch: A basin analysis, Sedimentary Geology, 40, 169–189, https://doi.org/10.1016/0037-0738(84)90045-9, 1984.

Wittmann, H. and vonBlanckenburg, F.: Cosmogenic nuclide budgeting of floodplain sediment transfer, Geomorphology, 109, 246–256, https://doi.org/10.1016/j.geomorph.2009.03.006, 2009.

905 Wittmann, H., Oelze, M., Gaillardet, J., Garzanti, E., and Blanckenburg, F. von: A global rate of denudation from cosmogenic nuclides in the Earth's largest rivers, Earth-Science Reviews, 204, 103147, https://doi.org/10.1016/j.earscirev.2020.103147, 2020.

Wittmann, H., Blanckenburg, F. von, Maurice, L., Guyot, J. L., and Kubik, P. W.: Recycling of Amazon floodplain sediment quantified by cosmogenic 26Al and 10Be, Geology, 39, 467–470, https://doi.org/10.1130/G31829.1, 2011.

910 Wittmann, H., vonBlanckenburg, F., Guyot, J. L., Maurice, L., and Kubik, P. W.: From source to sink: Preserving the cosmogenic 10Be-derived denudation rate signal of the Bolivian Andes in sediment of the Beni and Mamoré foreland basins, Earth and Planetary Science Letters, 288, 463–474, https://doi.org/10.1016/j.epsl.2009.10.008, 2009.

Yanites, B. J., Tucker, G. E., and Anderson, R. S.: Numerical and analytical models of cosmogenic radionuclide dynamics in landslide-dominated drainage basins, J. Geophys. Res., 114, https://doi.org/10.1029/2008JF001088, 2009.

915 Zimmermann, M., Perren, B., and Fehr, S.: Verbau Gürbe im Gebirge, Erneuerung und Unterhalt: Überprüfung der Wirksamkeit und der Wirtschaftlichkeit, IMPULS AG and NDR Consulting GmbH, Thun, 2016.